https://doi.org/10.1016/j.ijmecsci.2022.107672

Complex unloading behavior of titanium alloy in cold and thermal-mechanical working

J. Ma [a, b], H. Li [a, *], Z.R. He [a, c], H. Yang [a], M.W. Fu [b, **]

[a] State Key Laboratory of Solidification Processing, School of Materials Science and Engineering, Northwestern Polytechnical University, Xi’an, 710072, China.
[b] Department of Mechanical Engineering, The Hong Kong Polytechnic University, Hung Hom, Kowloon, Hong Kong, China.
[c] Chengdu Aircraft Industry (Group) Corporation Ltd., Chengdu 610092, China.
[*, **] Corresponding authors:
liheng@nwpu.edu.cn (Prof. H. Li); mmmwfu@polyu.edu.hk (Prof. M.W. Fu)

Abstract

Unloading behavior is of crucial importance in metal forming, which particularly creates a challenge to springback analysis and control of manufactured components. For working with hard-to-form materials at elevated temperatures, the thermal-mechanical coupling effect makes the unloading process more complicated and thus more difficult to model and control. Establishing an insight into the thermal-mechanical unloading behavior is crucial for ultimately improving the dimensional accuracy of formed components. In this work, using a near-alpha high-strength titanium alloy as a case, a series of continuous loading-unloading-reloading experiments within cold and warm forming domains were designed. Through the experiments, the complex unloading behavior, with a focus on the temperature-dependent degradation effect of elastic modulus and nonlinear stress-strain response, was investigated. A physically-based model was developed to reproduce the temperature-dependent nonlinear reduction effect of elastic modulus. In this model, the reversible mobile dislocation density is particularly included and modeled, thus accounting for the evolving nonlinear elastic strain component upon unloading with respect to both plastic strain and deformation temperature. Via model-based analysis, the mechanism accounting for the complex unloading nonlinearity in thermal-mechanical working is discussed from different evolutions of dislocation behaviors depending on plastic deformation and temperature.

Keywords: nonlinear unloading; thermal-mechanical working; springback prediction; physically-based modeling; dimensional accuracy

1. Introduction

Springback-induced dimensional deviation is one of the most quality issues in deformation-based manufacturing processes for metallic parts and components [1]. Springback mainly occurs at the end of a forming operation when the external loads are removed from the deformed materials. As a result, both the processing history and the unloading process will significantly affect the springback of the deformed parts [2–4]. Many metallic materials that have suffered plastic deformation normally do not follow the conventional linear elasticity theory during unloading, however, they present a nonlinear phenomenon [5–9]. Nonlinear unloading behavior makes prediction and control of springback more challenging. Springback prediction accuracy crucially depends on the accurate modeling of forming (loading) and unloading processes [2], where it would be more critical with the nonlinear elastic behaviors during unloading [10]. Despite its significant influence on springback and a lot of reported studies, there is still a lack of understanding of the complex nonlinear unloading phenomenon. Particularly for thermal-mechanical processing of hard-to-deform materials like high-strength titanium alloys, the thermal-mechanical effect complicates the unloading process and makes it more difficult to model and control springback [11,12]. Hence, the unloading behavior in thermal-mechanical working is becoming an imperative issue that needs to be addressed as it directly affects the determination of process parameters and the assurance of property and quality in deformation-based manufacturing processes.

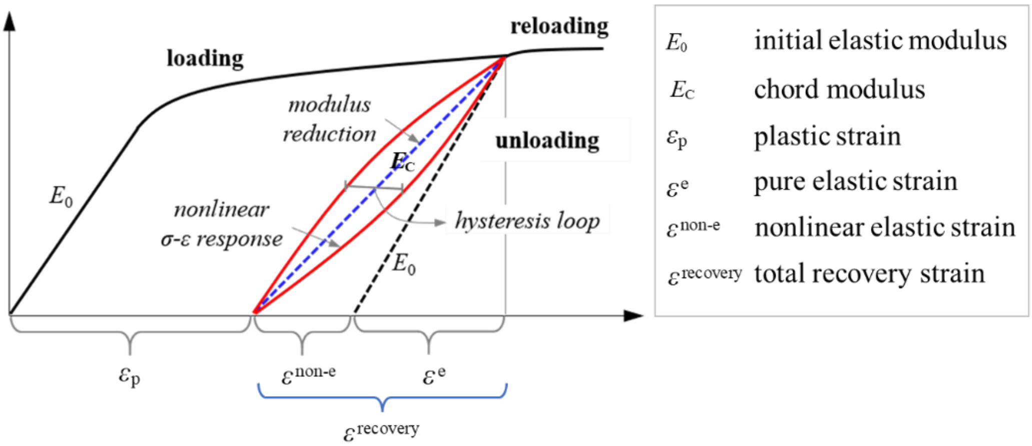

Fig. 1. Schematic of the nonlinear unloading behavior (based on [2]).

Nonlinear unloading behavior following the plastic deformation of metallic materials can be generally characterized by using the loading-unloading experiments such as tension loading-unloading-reloading (LUR), cyclic three-point bending, biaxial LUR, etc. [13–15]. A typical schematic graph of the stress-strain relationship in the LUR test is shown in Fig. 1. It is observed that the nonlinear unloading behavior includes two aspects, i.e., the nonlinear stress-strain response upon unloading and reloading, and the strain-dependent reduction of chord modulus (modulus reduction effect). The nonlinearities in unloading/reloading result in an elastic hysteresis loop, which indicates the energy dissipation during the process [13]. The modulus reduction effect means that the chord modulus obtained from the start to the end of an unloading-reloading curve presents a pronounced degradation phenomenon with increasing plastic deformation. The modulus reduction is different with material, grain size, straining level, temper condition, and loading path [15–18], but is less sensitive to strain rate within the static and intermediate strain rate range [19]. Of course, it should be noted that nonlinear unloading behavior is more complex than the above-mentioned points; for example, the nonlinearity in the elapsed-time dependency of springback (time-dependent springback) reported in many types of alloys [20–22], should also be included in this scope. In this study, we mainly focus on studying the unloading process when removing the external loads, but the time-dependent springback is not discussed yet.

Regarding the mechanisms behind the nonlinear unloading behavior, researchers have proposed many explanations. The typical ones include second-order elasticity caused by atomic bond stretching [23], inhomogeneous inner residual stress [24], deformation-induced texture evolution [25], damage evolution [26], twinning and detwinning or kink bands in HCP alloys [27], and dislocation interactions [5]. Among them, the pile-up and short-range reversible movement of dislocations have been accepted as the most significant mechanism of nonlinear unloading. During plastic deformation, sources of dislocation can be activated, and then numerous dislocations are thus created and also move along different slip planes in the materials. The dislocation structures impeded by the pinning obstacles such as grain boundaries, sub-cells, and solute particles, or the dislocations that pile up near the grain boundaries, can move to a new equilibrium with the relaxation of the lattice stress and thus create extra microscopic strain [28]. In some literature, such microscopic strain is known as micro-plastic strain [29] or quasi-plastic-elastic strain (QPE strain) and is also called anelastic strain at the macroscale level in many cases [13].

To model the nonlinear unloading phenomenon for predicting springback accurately as well as understanding the underlying mechanisms, some attempts have been made. According to whether the physical mechanism is considered, these constitutive models are categorized as phenomenologically-based models and physically-based ones. The phenomenological methods are mainly based on the well-known Hooke’s law, treating the loading/reloading as a linear process, using chord modulus-based functions of plastic strain to represent the plastic straining induced modulus degradation [30,31]. Examples include bilinear functions, three-stage-form functions, polynomial functions, power functions, exponential forms, and some others. Among them, an exponential model proposed by Yoshida and Uemori has attracted extensive applications in the springback analysis, thanks to the advantages in parameter identification, implementation, and computation efficiency in FE simulation [30]. However, since it approximates the unloading stress-strain curve as a linear chord, the model will lose some accuracy when the material is not completely unloaded due to the difference between the chord line and the nonlinear unloading curve. In practical forming cases, the locally uncompleted unloading commonly exists and can result in non-uniformly distributed residual stresses in the formed part after global unloading [29,32]. To well represent the nonlinear unloading, several other models were proposed by introducing the unloading stress as an additional variable in the functions of chord modulus [33,34]. In addition, some most recent models are also proposed to capture the nonlinear stress-strain response upon loading/reloading, such as the Yoshida-Uemori model [35], multi-surface model [36], QPE (quasi-plastic-elastic) model [13], and one surface model [37]. Additionally, several models have been developed from the aspect of the dislocation-dominated mechanism within continuum dislocations dynamics (CDD). For instance, a dislocation-based model was recently proposed to describe the microplastic strain in the pre-yield regime [28,38]. Different from the pure elastic deformation caused by the inter-atomic bond, the pre-yield claims that the bowing-out of dislocation segments can contribute to creating microplastic strain at the same time during loading. So, the density of dislocation and the length of dislocation segments were used in the above model to describe the microplastic strain component. Based on this understanding, Torkabadi et al. [39] developed a semi-physical model to describe the nonlinear elastic behavior and applied it to the description of nonlinear loading-unloading curves of AHSS in cold forming. In that model, the recoverable anelastic strain is proportional to the dislocation density, and the Taylor equation is adopted to associate the dislocation density with the flow stress. In addition to the works reviewed above, several attempts in discrete dislocation dynamics simulation and molecular dynamics simulation for studying the nonlinear unloading behavior have been made recently [40,41].

The body of study on nonlinear unloading is more extensive than the above-summarized ones and many not mentioned do have made great contributions to understanding the unloading behavior and underlying mechanisms. However, these works mainly focus on cold deformation. For the unloading behavior under thermal-mechanical working, little attention has been received, which limits the effective analysis of springback in metal forming at elevated temperatures. For thermal-mechanical working, some high-strength, difficult-to-deform materials can still present a high strength-to-modulus ratio; for example, the ratio of the high-strength Ti-alloys within the warm forming domain can be up to about 2.5~3 times higher than the widely used advanced high strength steels (AHSS) in the cold forming domain, leading to remarkable springback during forming at elevated temperatures. The unloading at elevated temperatures, whether it has similar nonlinear characteristics to cold forming or any other different phenomena, remains unknown. In addition, the complex thermal-mechanical history makes the unloading process in deformation at elevated temperatures more complicated and more difficult to represent. Therefore, characterizing and modeling the nonlinear unloading behavior within the temperature range from cold to warm domains is a challenging issue to be explored.

To fill the identified research gaps, this paper aims at exploring the nonlinear unloading behavior within cold and warm deformation domains and establish insight into the evolving unloading behavior under thermal-mechanical working. First, by taking the near-alpha high-strength titanium alloy as a case, continuous loading-unloading-reloading tests are designed and performed to explore the temperature-dependent evolution of nonlinear unloading from cold to warm domains. Furthermore, from the aspect of dislocation interactions upon loading/unloading, a physically-based model with the reversible mobile dislocation introduced is established and assessed for understanding of the unloading behavior. Finally, the evolution behaviors of dislocations with plastic strain and deformation temperature are analyzed, and the mechanism for nonlinear unloading behavior in cold and thermal-mechanical working is discussed.

2. Design of experiment

2.1. Material

In this research, high-strength Ti-3Al-2.5V tubular material (HSTT), with a nominal outer diameter of 6 mm and a nominal thickness of 0.5 mm, is used as the case material. Ti-3Al-2.5V is a typical near-alpha titanium alloy and its nominal chemical compositions are shown in Table 1. The as-received Ti-3Al-2.5V tube is manufactured by multi-pass cold-rolling and then treated as the stress-relieved condition according to SAE 4946 [42]. The reason for using tubular specimens is due to that the unloading-induced springback analysis is a challenging issue in tube bending processes. For high-strength titanium tubes, there are two significant problems seriously affecting the bending process—one is the limited bendability due to its low ductility, and another is the significant springback due to its high strength-to-elastic modulus ratio even at elevated deformation conditions. In previous research, a novel bending method so-called locally differential heating-assisted bending method was developed, which enables tight-radius bending of high-strength titanium tubes [12]. However, springback is still remarkable in heating-assisted bending and is more difficult to predict and control as compared to cold deformation due to the temperature-dependent unloading behavior. Therefore, clarifying the complex unloading behavior under cold and thermal-mechanical working will contribute to accurately solving the springback problem in heat-assisted tube bending.

Table 1 Chemical compositions of Ti-3Al-2.5V tubular material (weight %)

Material	N	C	H	O	Fe	N	Al	V	Ti
Ti-3Al-2.5V	0.02	0.05	0.015	0.12	0.3	0.02	2.5-3.5	2.0-3.0	balance

Fig. 2 shows the material microstructure obtained by the EBSD test on the normal direction (ND)-rolling direction (RD) plane with respect to the traverse direction (TD). The average grain size is about 1 μm. The alpha phases with elongated wrought structures dominate the microstructure, and some minor partially transformed beta phases also exist in the boundaries of alpha grains. The inverse pole figure indicates a near radial texture (<0001>//ND) in the tubular material. For the HCP-structured Ti-alloy, both gliding and twinning modes concurrently contribute to the plastic deformation [43]. In addition, Li et al. [44] revealed that the maximum volume fraction of twinning is about 0.8% in tension and 2.6% in compression, respectively, which indicates that dislocation gliding is the most significant mechanism to accommodate plastic strain. In the following modeling work, the twinning mode is thus ignored, and the dislocation interactions are considered in both loading and unloading processes.

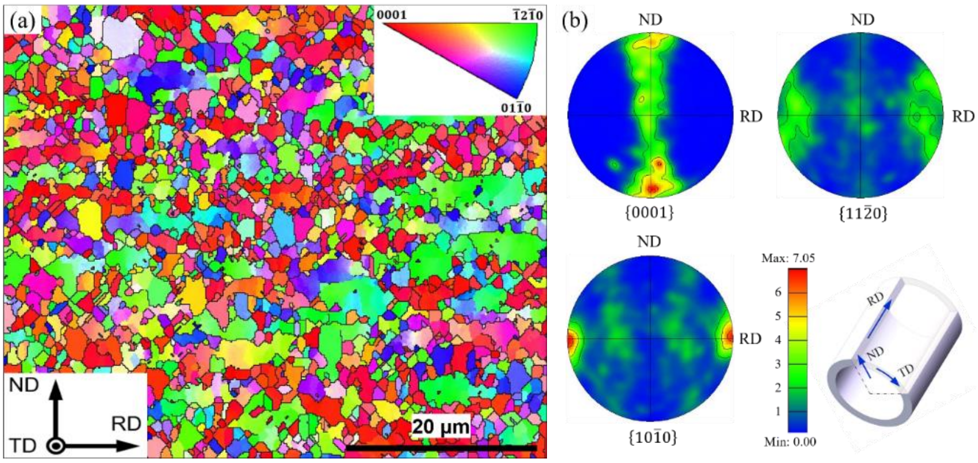

Fig. 2. Microstructure characteristics of the as-received Ti-3Al-2.5V tubular material: (a) EBSD orientation map; (b) Pole figure.

2.2. Mechanical Characterization

Uniaxial tension tests in the RD of the tubular materials are performed at room and elevated temperatures according to the standards of ASTM E8 [45] and ASTM E21 [46]. First, two round insert parts were placed inside the tube clamp area. The geometrical dimensions of the round insert parts were designed and manufactured according to ASTM E8. Second, the tube specimen with inset parts inside the clamp areas was clamped by using manual serrated wedge gripers. Third, the tube specimen together with the gripper units were placed inside the oven for tensile tests at elevated temperatures. However, as the tensile tests in this study were carried out at high temperatures up to 400℃, the grippers were specially designed and made by Ni-based superalloy K403 (as shown in Fig. 3 (a)), hence ensuring the clamp stability at elevated temperatures. The tests are conducted at a nominal strain rate of 0.001 s^{-1}, and the gauge length of the testing sample is 50 mm (as shown in Fig. 3 (b)). To measure the deformation at various temperatures, Epsilon Class B (3448-050M-020) high-temperature extensometer with +20% / -10% gauge range (Fig. 3 (a)) is used to measure the elastic-plastic strain in uniaxial tension experiments of HSTT at different temperatures. This extensometer can be used at a very high temperature up to 1200 °C and has a high resolution. By using the displacement measured by the extensometer and the load registered by the test machine, as well as taking the cross-sectional area into account, the engineering strain (ε_{eng}) and engineering stress (σ_{eng}) can be calculated. Then, the true stress can thus be obtained from the engineering stress using the equation $\sigma_{\text{true}} = \sigma_{\text{eng}}(1 + \varepsilon_{\text{eng}})$. Fig. 4 shows the true flow stress from 20 to 400 °C, in which the experimental data are fitted by the Swift hardening function to provide a unified description for the identification of model parameters.

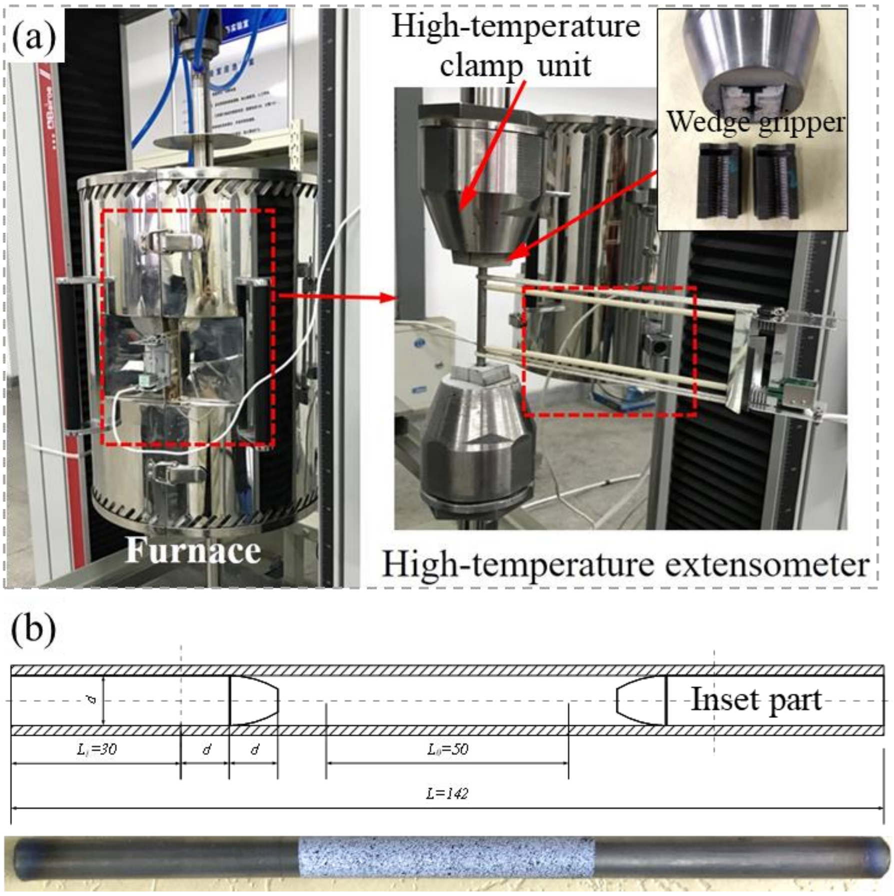

Fig. 3. High-temperature mechanical testing: (a) testing platform assembly; (b) tubular tensile specimen

To characterize the unloading behavior under thermal-mechanical deformation, the continuous tension loading-unloading-reloading (LUR) tests with several cycles at cold and warm temperatures of 20~400 °C are conducted. Similar to the tension test, several engineering strain points are pre-defined as the unloading positions in the LUR test. The testing sample is loaded to a pre-set strain position and then reversely unloaded to the zero-stress state, and then reloaded to the next pre-set strain position. In the loading process, the displacement-control method (equivalent to the engineering strain rate of about 0.001 s^{-1}) is also applied. The load-control method with 200 $N\cdot s^{-1}$ is adopted in the unloading process to avoid the over-large decrease of flow stress using the displacement-control method upon unloading. The corresponding true strain positions are as set as [0.01, 0.013, 0.018, 0.025, 0.034, 0.055, 0.067, 0.08, 0.1, 0.12, 0.14, 0.16].

3. Characterization results of unloading behavior

3.1. Nonlinear unloading behavior at room temperatures

As mentioned previously, the nonlinear elasticity can be categorized as the nonlinear stress-strain response upon unloading and the modulus reduction effect with the accumulation of plastic strain. Based on the tension loading-unloading-reloading test at room temperature, the stress-strain curve of high-strength titanium alloy is shown in Fig. 4. It can be found that the stress-strain response during unloading and reloading is far from a straight line. In a loading-reloading cycle, the stress-strain curve upon reloading legs behind the curve upon unloading, and thus comes out with a hysteresis loop. For the higher flow stress or the larger strain level, a more pronounced hysteresis loop can be observed. In this section, the nonlinear unloading behavior in the cold forming will be analyzed from the aspects of nonlinear stress-strain response and modulus reduction effect.

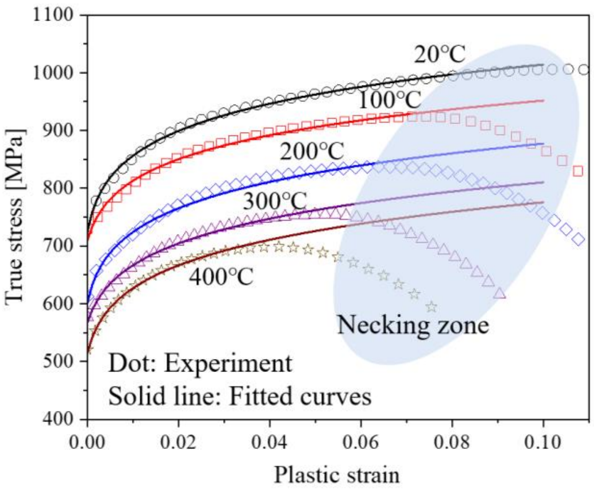

Fig. 4. True stress *vs* plastic strain curves at different temperatures.

3.1.1. Nonlinear unloading stress-strain response

Comparing the uniaxial tension result with the flow stress of LUR, it can also be found from Fig. 5 that the re-yield strength is slightly greater than the uniaxial tension stress and then trends to be the same as the tension stress. Similarly, the stress difference between reloading and uniaxial loading is increased with the increase of flow stress. The maximum stress difference is about 18 MPa with the strain of about 0.08, which takes up about 1.7% of its current flow stress. In general, reloading just creates a very minor effect on the magnitude of reloading flow stress and thus can be ignored in the overall analysis of the unloading nonlinearity.

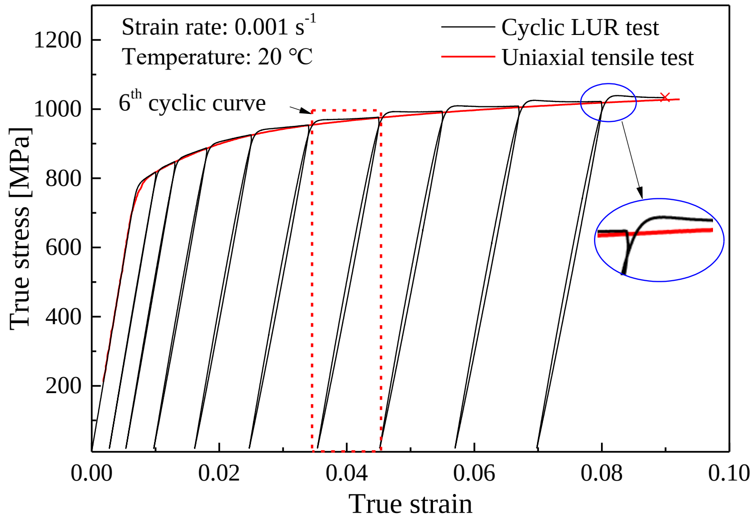

Fig. 5. Stress-strain responses of cyclic loading-unloading-reloading tests of Ti-3Al-2.5V alloy.

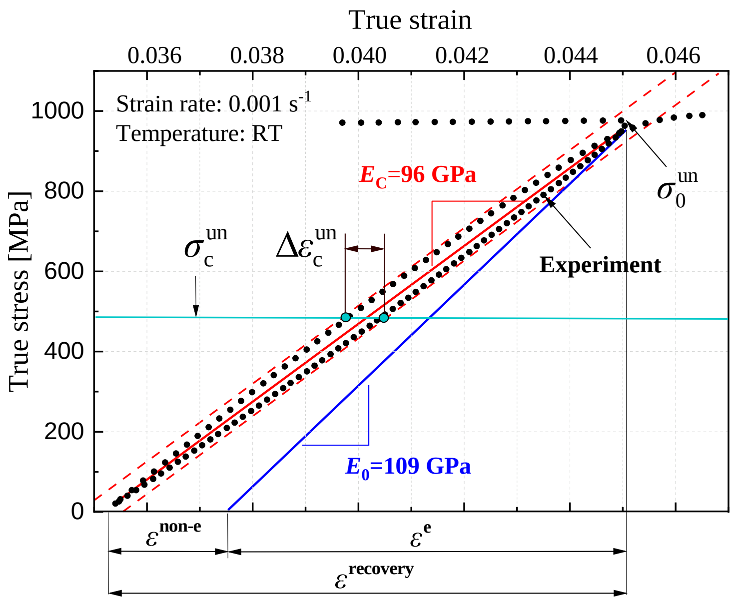

Fig. 6. Stress-strain response of a single loading-unloading-reloading loop (the 6th from Fig. 5) of the Ti-3Al-2.5V tube at room temperature

Furthermore, the unloading-reloading curves and moduli were analyzed in detail. It is noted that the linear fitting method was employed to fit the stress-strain curve within the elastic scope under initial loading, thus determining the initial Young's modulus. During the linear fitting, the zero-stress point was selected as the lower limit. For the upper limit, it is difficult to find a very exact point. In this study, several points close to but below the yielding were firstly selected as the trial upper limits for linear fitting. By averaging the fitted Young's moduli obtained from several trials, the initial Young's modulus was thus determined. For the chord moduli during unloading under different pre-strains, the modulus values were determined by calculating the slope of the chord line between the two cross points of unloading and reloading curves. In such a way, the initial modulus and the chord moduli under different pre-strain levels can be obtained from Fig. 5.

As shown in Fig. 6, taking the sixth cycle of LUR from Fig. 5 for further analysis, it can be seen from the magnified view of the stress-strain curve that both the unloading and reloading stress-strain relationships are nonlinear. The reloading curve seems to be an inverse process to the unloading. In Fig. 6, the initial unloading stress (σ_0^{un}) represents the stress at the start point of unloading (equivalent to the flow stress prior to unloading), and E_0 and E_C represent the initial elastic modulus obtained from the uniaxial tension test and the chord modulus of the given unloading-reloading loop. As shown in Fig. 6, the chord modulus at the strain of 0.045 is about E_C=96 GPa. As compared with the initial elastic modulus (E_0=109 GPa), the chord modulus is reduced by about 12%. As the actual unloading and reloading curves are nonlinear, the corresponding strains for unloading and reloading at the same stress level are different. The strain difference increases gradually along with the decrease of the stress upon unloading and reaches a maximum value ($\Delta\varepsilon_{\mathrm{c}}^{\mathrm{un}}$) when the stress decreases to a critical state—approximate half of the initial unloading stress (σ_0^{un}), as shown in Fig. 6. After then, the strain difference decreases gradually to zero when the actual stress is unloaded to zero. Thus, half of the initial unloading stress is defined as the critical unloading stress ($\sigma_{\mathrm{c}}^{\mathrm{un}}$) to represent a state where the maximum strain difference is in an unloading-reloading loop. For the unloading-reloading loop shown in Fig. 6, the critical unloading stress is about $\sigma_{\mathrm{c}}^{\mathrm{un}} = 490\ \mathrm{MPa}$. Since the chord line approximately divides the loop into two same parts, the deviation of the unloading strain calculated by the chord modulus to actual unloading is also the maximum at this critical state. Additionally, the total recovery strain during unloading can be calculated as $\varepsilon^{\mathrm{recovery}} = 0.0096$. If using the initial elastic modulus for calculation, the recovery strain is called pure elastic unloading strain and is ε^{e}=0.0075. By comparing the two values, one could calculate the component of nonlinear elastic unloading strain is $\varepsilon^{\text{non-e}} = 0.0021$, which takes about 21% of the total recovery strain.

Furthermore, the instantaneous gradient of modulus during unloading at different pre-strains is analyzed. Fig. 7 shows the variation of instantaneous gradient among the pre-strains of 0.018, 0.045, and 0.080. The *x*-axis (horizontal) and *y*-axis (vertical) are normalized by using the initial unloading stress (σ_0^{un}), and the initial elastic modulus (E_0), respectively. For all the three cases with different pre-strain levels, the instantaneous gradients quickly decrease at the start of the unloading process, then gradually decrease near-linearly to the zero-stress state (at the end of the unloading process), which shows that there is no definite linear part in the entire unloading process. The overall tendency of instantaneous gradient agrees with the nonlinear unloading studies in aluminum alloys, mild steels, and magnesium alloys reported by several previous works [7,29,33]. When focusing on the beginning of unloading, it is found that the dramatic decrease of the gradient is similar to that in magnesium alloys. However, such a dramatic decrease of the gradient at the beginning can hardly be found for aluminum alloys and mild steels [7].

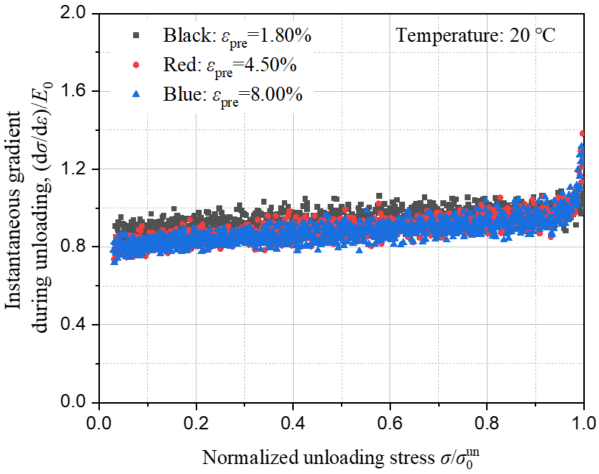

Fig. 7. Variation of the instantaneous gradient of modulus during unloading at different pre-strains in cold deformation.

It also can be observed from Fig. 7, that, when comparing the gradients of the near-linear stage under three pre-strains, we can find that the overall gradient level at 0.018 pre-strain is much higher than those at the other two pre-strains. However, the overall gradient level at 0.045 pre-strain is only very slightly higher than that at 0.080 pre-strain, even though the pre-strain of the former is much smaller than the latter. This phenomenon shows that the degree of the nonlinearity in the stress-strain response upon unloading is increased with the increase of pre-strain, and then gradually tends to be saturated when the pre-strain reaches a certain level. In addition, except for the beginning stage of the unloading process, it can be found that the normalized modulus in the near initial unloading stage is approximately equal to one. That is to say, the transient unloading modulus at this point equals the initial elastic modulus of the material. With the unloading proceeds, the transient unloading modulus gradually reduces to a smaller value until the external load is removed.

3.1.2. Strain-related reduction of unloading modulus

Fig. 8 demonstrates the chord modulus at various plastic strains. It can be seen that the chord modulus is significantly decreased once the material suffers plastic deformation, and the reducing rate becomes slow and slow with the continuous accumulation of plastic strain. When the strain is about 0.05, the chord modulus seems to be saturated at 91 GPa. The maximum reduction of chord modulus is about 18 GPa, which takes up about 16.5% of the initial elastic modulus. Actually, the modulus reduction effect has been widely observed in many metals and alloys, but the reduction amount of modulus varies with different materials. For example, the reported maximum reduction can be up to about 22% in AHSS [47], 11% in aluminum [29], 20% in copper [48], and 14% in titanium [6], as compared to their initial modulus values.

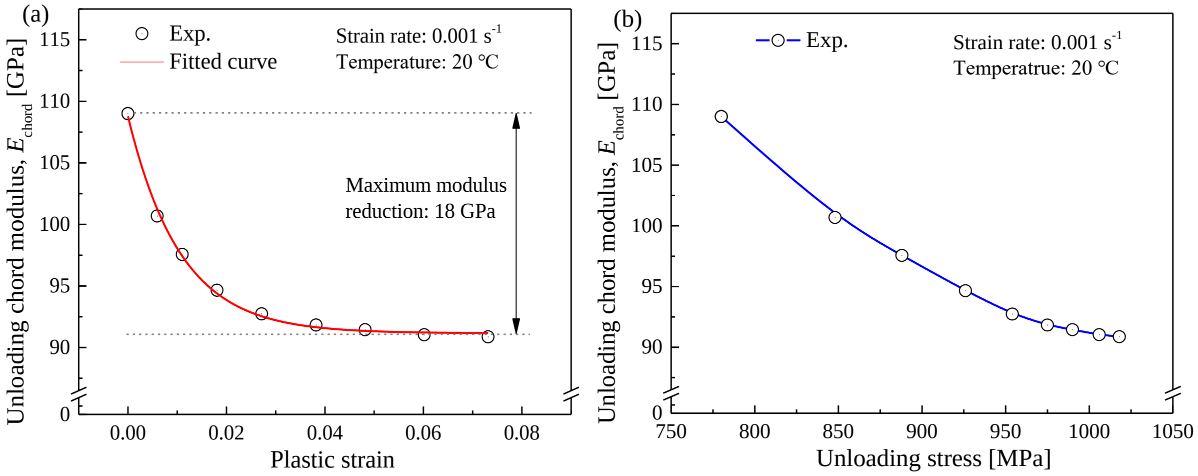

Fig. 8. Modulus reduction effect of Ti-3Al-2.5V alloy at room temperature: (a) Chord modulus *vs*. plastic strain; (b) Chord modulus *vs*. unloading stress.

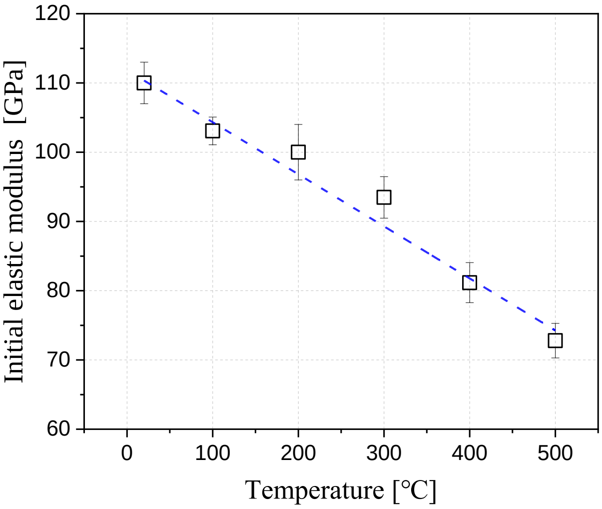

Fig. 9. Elastic modulus at various temperatures of Ti-3Al-2.5V alloy.

3.2. Nonlinear unloading behavior at elevated temperatures

Warm forming is conducted at the elevated temperature above room temperature but below the recrystallization temperature of the material. Section 3.1 introduces the nonlinear unloading behavior of titanium materials at the cold forming domain. However, how the unloading nonlinearity evolves with increasing the forming temperature is not yet known. In this Section, the temperature-dependent evolution of nonlinear unloading behavior will be discussed based on LUR tests at elevated temperatures.

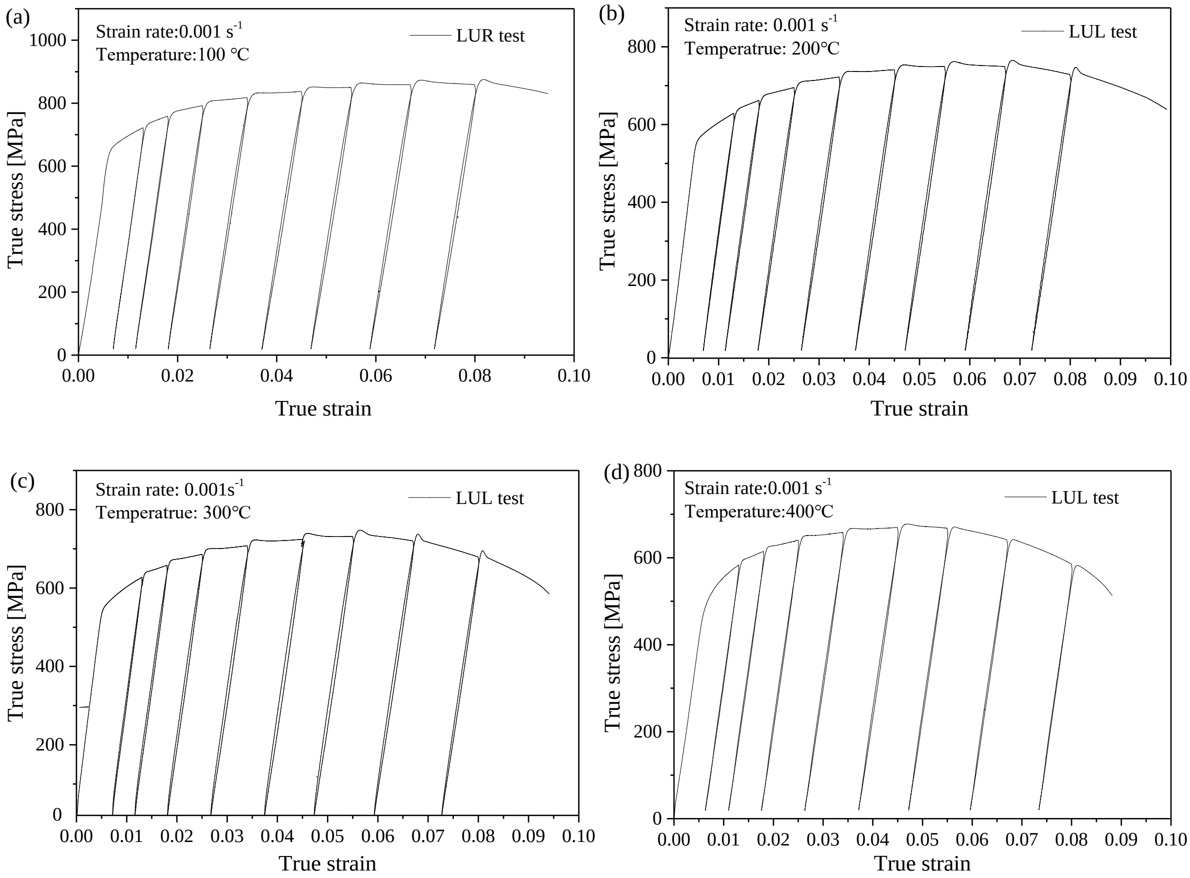

Fig. 10. Stress-strain responses of the cyclic tension LUR tests of Ti-3Al-2.5V alloy at elevated temperatures: (a) 100°C; (b) 200°C; (c) 300°C; (d) 400°C.

3.2.1. Temperature-dependent initial elastic modulus

From the view of the micro-scale, the elastic modulus is a representation of the interaction force of the bonded atoms in materials. Normally, material elasticity property can be measured by mechanical tests such as the uniaxial tensile test, ultrasonic pulse-echo technique, and resonant frequency damping method. By analyzing the stress-strain curves obtained from the uniaxial tension tests within the cold and warm forming regimes, the initial elastic moduli of the case titanium alloy of this research at different temperatures can be obtained, as shown in Fig. 9. It is observed that the elastic modulus decreases at a near-linear trend, as the forming temperature increases. From 20 to 400 °C, the elastic modulus is decreased by 25.7% from 109 to 81 GPa. Such a linear decrease phenomenon depending on temperature has also been reported previously in an alpha-titanium polycrystal [49]. The temperature-dependent change of elastic modulus is a well-known phenomenon and has been widely observed in most metallic materials. The reduction of elastic modulus may present nonlinear trends with temperature, depending on the materials and the applied temperature ranges. Elasticity originates from the interaction forces between the atoms of the solids under deformation, and therefore the general nature of the atomic bonding affects the elastic property. When the temperature of the material is increased, the atomic thermal vibration is increased accordingly, which will lead to changes in lattice potential energy and curvature of the potential energy curve, and therefore, the elastic modulus will change [50].

3.2.2. Temperature-dependent nonlinear stress-strain response

Fig. 10 illustrates the stress-strain curves obtained from the LUR tests at different elevated temperatures. It is found that the stress-strain responses in the warm forming domain are similar to that in cold forming. Both the unloading and reloading curves are nonlinear. The subsequent reloading curve lags behind the unloading curve, forming a hysteresis loop at each unloading-reloading circle.

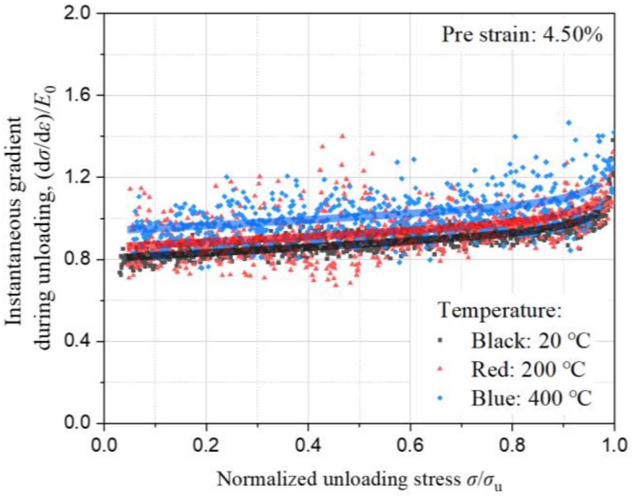

Fig. 11. Variation of the instantaneous gradient of modulus during unloading at the pre-strain of 4.50% for different deformation temperatures.

In addition, to make a more detailed analysis of the temperature-dependent unloading behavior, the instantaneous gradient is also discussed. Fig. 11 illustrates the instantaneous gradients at the pre-strain of 4.50% under the deformation temperature range of 20~400℃. It should be noted that the data dots at room temperature is well convergent, while the data dots obtained at elevated temperatures looks relatively scattered. The reason may be attributed to the stability of the experiment, where the experiments at elevated temperatures are more sensitive to being affected by variation of parameters. From the overview of the statistical distribution of the data dots, however, the temperature-dependent characteristics of the instantaneous gradient can still be observed. With the increase of deformation temperature, the overall gradient level is increased, thus showing that the nonlinearity of stress-strain upon unloading is lower at higher temperatures.

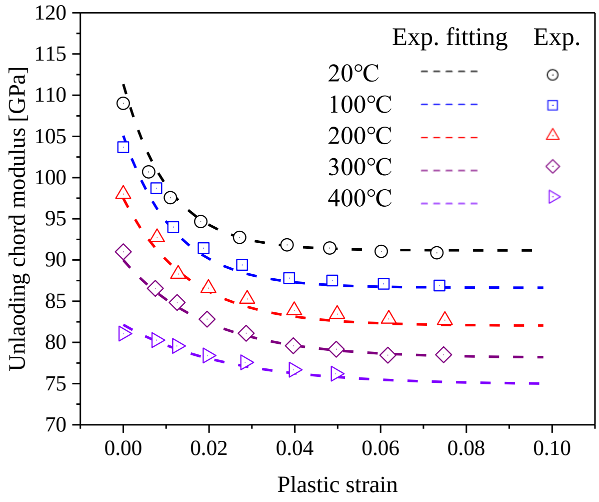

Fig. 12. Modulus reduction effect with plastic strain at elevated temperatures.

3.2.3. Temperature-dependent modulus reduction effect

As shown in Fig. 12, both the temperature and plastic strain present a significant effect on the chord modulus of high strength Ti-3Al-2.5V tube. At the temperature range of 100~300℃, the chord modulus exhibits an exponential decaying trend and then becomes saturated when the strain exceeds about 5%. Increasing the deformation temperature, the maximum reduction of chord modulus becomes smaller. For the cold forming, the modulus reduction percentage is about 18%. At 300℃, the modulus reduction percentage is reduced to about 14%. At 400℃, however, the reduction percentage of the chord modulus is reduced to about 6%.

4. Physically-based modeling

To construct a physically based model for studying the temperature-dependent nonlinear unloading phenomena, this section introduces the derivation of nonlinear elastic strain and plastic flow stress, the concept of reversible mobile dislocation, and dynamic equations of mobile/immobile dislocations, and their temperature/rate dependences.

4.1. Derivation of nonlinear elastic strain and flow stress

In metallic materials, dislocations can be categorized into two types: mobile and immobile. The former in plastic deformation accommodates plastic strain, while the latter mainly contributes to the working-hardening of plastically deformed materials. As illustrated in Fig. 13, the dislocations are nonuniformly distributed in grains and grain boundaries (GB). In terms of their arrangement, the total dislocations in metals can be categorized as cell dislocations and wall dislocations. The wall dislocations locate within the cell boundaries (CB) and are immobile, however, the cell dislocations can be either mobile or immobile depending on their locations. These cell dislocations distributed statistically inside the sub-cells (SC) are normally mobile; however, those forest dislocations stored in the incidental dislocation boundaries (IDB) are normally immobile. Both immobile dislocations (cell and wall) contribute to the work-hardening during plastic deformation. The densities of the above dislocations can be described as follows:

$$\begin{cases}\rho_{\text{t-cell}}=\rho_{\text{m-cell}}+\rho_{\text{im-cell}}\\ \rho_{\text{t-wall}}=\rho_{\text{im-wall}}\end{cases} \tag{1}$$

where $\rho_{\text{t-cell}}$ and $\rho_{\text{t-wall}}$ represent total cell and wall dislocation densities, respectively. The former is composed of mobile cell dislocations ($\rho_{\text{m-cell}}$) and immobile ones ($\rho_{\text{im-cell}}$), and the latter is only composed of immobile wall dislocations ($\rho_{\text{im-wall}}$).

From the view of the mobility property of dislocations, Eq. (1) can be re-written as follows:

$$\begin{cases}\rho_{\text{m}}=\rho_{\text{m-cell}}\\ \rho_{\text{im}}=\rho_{\text{im-cell}}+\rho_{\text{im-wall}}\end{cases} \tag{2}$$

Thus, the total dislocation density can be expressed by:

$$\rho_{\text{t}}=\rho_{\text{t-cell}}+\rho_{\text{t-wall}}=\rho_{\text{m}}+\rho_{\text{im}} \tag{3}$$

As plastic deformation occurs prior to unloading, the flow stress along with plastic strain needs to be modeled first. In this research, based on the plasticity theory of polycrystalline materials developed by Kocks [51], a temperature-dependent governing equation for flow stress is constructed, and shown in Appendix A. Here the following mainly focuses on the derivation of governing equation for nonlinear elastic strain during unloading.

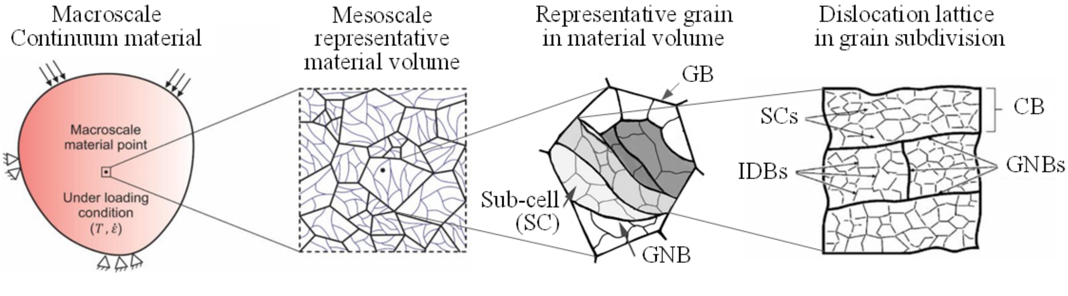

- (Immobile) wall dislocations ($\rho_{\text{im-wall}}$) : locate within the cell boundaries (CB)
- Mobile cell dislocations ($\rho_{\text{m-cell}}$): distributed statistically inside the sub-cells (SC)
- Immobile cell dislocations ($\rho_{\text{im-cell}}$): stored in the incidental dislocation boundaries (IDB)

Fig. 13. Schematic of dislocation arrangement in metallic materials (based on [52,53])

To begin with the derivation of equations, several definitions need to be declared, i.e., total recovery strain ($\varepsilon^{\text{recovery}}$), pure elastic strain (ε^{e}), and nonlinear elastic strain ($\varepsilon^{\text{non-e}}$), as illustrated in Fig. 1. More detailed explanation can also be found in Section 3.1.1. So, the total recovery strain is composed of two components, i.e., pure elastic strain and nonlinear elastic strain, as designated by:

$$\varepsilon^{\text{recovery}} = \varepsilon^{\text{non-e}} + \varepsilon^{\text{e}} = \varepsilon^{\text{non-e}} + \sigma_f / E \tag{4}$$

Thus, the nonlinear elastic strain can thus be denoted as:

$$\varepsilon^{\text{non-e}} = \varepsilon^{\text{recovery}} - \sigma_f / E \tag{5}$$

where *E* is the elastic modulus that can be obtained from the uniaxial tension tests and σ_f is the flow stress at the point where unloading starts. Accordingly, the nonlinear elastic strain with the plastic strain of titanium alloy at different temperatures can be calculated from Eq. (5), and shown in Fig. 14.

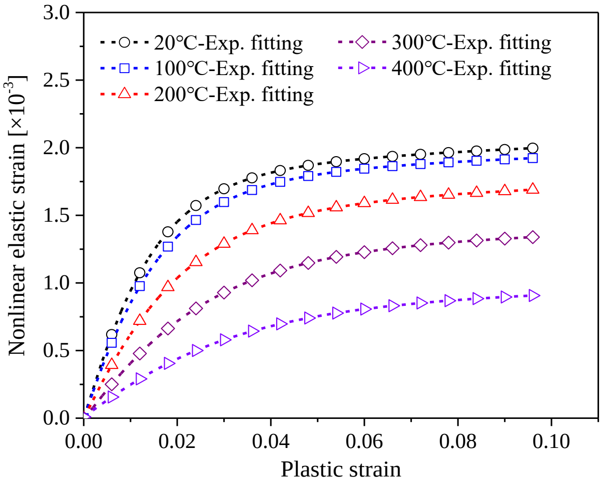

Fig. 14. Nonlinear elastic strain with plastic strain at different temperatures.

4.2. Evolution of reversible mobile dislocation density

4.2.1. Definition of reversible mobile dislocation

From the view of dislocation, the movement of mobile dislocations can induce the plastic strain, calculated by [54]:

$$\varepsilon_{\text{p}} = b\rho_{\text{m}}\bar{\Lambda} \tag{6}$$

where ρ_{m} is the density of mobile dislocations, *b* is Burger vector, and $\bar{\Lambda}$ is the dislocation mean free path.

However, the nonlinear elastic strain component, as described in Eq. (5), is caused by the short-range movement of these mobile dislocation segments, not all the mobile dislocations [28,55,56]. So, to distinguish their contributions, mobile dislocations can be divided into two categories, summarized as follows:

- One is irreversible mobile dislocations, which can completely move across the slip plane to contribute to a Burger's vector micro-strain to the macro-scaled plastic strain or be pinned up by nodes, composites jog, precipitates, etc. The pinned dislocation segment bows out during plastic deformation and acts as the Frank-Read source to create dislocation loops once the applied shear stress can reach the critical value.

- Another one is reversible mobile dislocations, which is the previously described pinned-up dislocation segment. For these segments, when the applied shear stress is below the critical value, the bow-out dislocations cannot become the Frank-Read source. In this case, when the external loads are removed or reduced, they will return to the original state or a condition with larger curvatures. These bow-out dislocation segments become reversible, thus leading to nonlinear elastic strain upon unloading.

Both the densities of two types of mobile dislocations, i.e., reversible one ($\rho_{\mathrm{m}}^{\mathrm{re}}$) and irreversible one ($\rho_{\mathrm{m}}^{\mathrm{irrev}}$), are used to distinguish their contributions to plastic strain and nonlinear elastic strain. Thus, the density of total mobile dislocations can be re-written as:

$$\rho_{\mathrm{m}}=\rho_{\mathrm{m}}^{\mathrm{irrev}}+\rho_{\mathrm{m}}^{\mathrm{rev}} \tag{7}$$

where the density of reversible mobile dislocations is assumed to take up a fraction η ($0 \leq \eta \leq 1$) of the density of total mobile dislocations, represented as:

$$\begin{cases} \rho_{\mathrm{m}}^{\mathrm{irrev}} = (1-\eta) \cdot \rho_{\mathrm{m}} \\ \rho_{\mathrm{m}}^{\mathrm{rev}} = \eta \cdot \rho_{\mathrm{m}} \end{cases} \tag{8}$$

By combing Eqs. (6) and (8), the nonlinear elastic strain can thus be re-written as:

$$\varepsilon^{\text{non-e}} = b \cdot \eta \cdot \rho_{\mathrm{m}} \cdot \bar{\Lambda} \tag{9}$$

It is known that the density of total mobile dislocation exhibits a complex evolution in the material forming process. At different strain levels, the irreversible mobile dislocation density is also different due to their mobility difficulty. Thus, both densities of irreversible reversible mobile dislocations evolve accordingly during the deformation process. In addition, the density of total mobile dislocation is affected by the deformation temperature and strain rate, which also, in turn, affects the irreversible and reversible components. Hence, this fraction can be written as a function of total mobile dislocation density (ρ_{m}), plastic strain (ε), strain rate ($\dot{\varepsilon}$), and deformation temperature (T), and thus can be briefly designated as:

$$\eta=\eta(\rho_{\mathrm{m}}, \varepsilon, \ \dot{\varepsilon}, T) \tag{10}$$

4.2.2. Evolution of reversible mobile dislocation

In metal forming processes, when the plastic deformation occurs, both the densities of mobile and immobile dislocations are increased first and then tend to be saturated along with the accumulation of plastic strain, and the increasing rate of mobile dislocation density is normally greater than that of immobile one [57]. The increased density of mobile dislocation thus provides a bigger possibility for creating plastic strain; meanwhile, the higher immobile dislocation density can make the mean free path decrease so the mobile dislocations become easier to be immobilized [58]. At the beginning of the plastic deformation stage, the density of mobile dislocations remains at a relatively low level, and most of them can act as dislocation sources to generate new dislocations under external forces [59]. Thus, only a part of the movements of mobile dislocations is reversible during unloading [60], which can contribute to the nonlinear elastic strain [38]. As deformation proceeds, increased mobile dislocations can support more reversible movements. At the same time, increased immobile dislocations shorten the spacing distance of immobile dislocations (mean free path of dislocations) so the mobile dislocation movement will gradually become difficult. Based on the above understanding, it is assumed that the reversible mobile dislocation fraction (η) is proportional to the density of mobile dislocations, but inversely proportional to the average spacing distance of immobile dislocations, as given by Eq. (11).

$$\begin{cases} \eta \propto \rho_{\mathrm{m}} \\ \eta \propto \left(1/\bar{\Lambda}\right) \end{cases} \tag{11}$$

where $\bar{\Lambda}$ represents the mean free path and it can be considered as a function of immobile dislocation density [61], as denoted by:

$$\bar{\Lambda} \propto \rho_{\mathrm{im}}^{-1/2} \tag{12}$$

By considering the effects of mobile and immobile dislocations on the fraction of reversible mobile dislocation density during the plastic deformation process, an equation can be proposed to describe this fraction parameter, as given by Eq. (13). In this equation, the effects of mobile and immobile dislocations are modeled by the second and third terms, respectively, together with the first term as a material coefficient. A form of function considering the increase of dislocation density as compared to the initial density before deformation is used to describe the effects of two densities on the density of reversible mobile dislocations.

$$\eta=\lambda^{\mathrm{rev}} \cdot \left(\frac{\rho_{\mathrm{m}} - \rho_{\mathrm{m},0}}{\rho_{\mathrm{m}}} \right) \cdot \left(\frac{\rho_{\mathrm{im}}^{-1/2} - \rho_{\mathrm{im},0}^{-1/2}}{\rho_{\mathrm{im}}^{-1/2}} \right) \tag{13}$$

where $\rho_{\mathrm{m},0}$ and $\rho_{\mathrm{im},0}$ are the initial densities of mobile and immobile dislocations of the material before deformation, and λ^{rev} is a material coefficient to represent the probability generation magnitude of reversible mobile dislocations. In thermal-mechanical working, the material coefficient λ^{rev} is dependent on the temperature. It was reported that a power-law equation can be used to describe the temperature-dependent variation of model coefficients related to the probability of thermal-affected dislocation behavior [53]. Thus, a phenomenological power equation is used to describe the temperature-dependent coefficient λ^{rev}, as given by:

$$\lambda^{\mathrm{rev}} = \lambda_{\mathrm{ref}}^{\mathrm{rev}} \left[1+\omega_{\mathrm{rev}} \left(\frac{T - T_{\mathrm{ref}}}{T_{\mathrm{ref}}} \right)^{r_{\mathrm{rev}}} \right] \tag{14}$$

where $\lambda_{\mathrm{ref}}^{\mathrm{rev}}$, ω_{rev} and r_{rev} are material coefficients that need to be determined.

4.3. Evolution of immobile and total mobile dislocation densities

4.3.1 Behaviors of mobile and immobile dislocations

During plastic deformation, both mobile and immobile dislocations evolve with plastic strain. Dislocation evolution behavior can be divided into dynamic and static evolutions, summarized as follows [53,62]: for the dynamic evolution of dislocation behaviors, there are six types of main sources to be considered in the modeling framework including multiplication, annihilation, trapping, accumulation, dislocations nucleation, and mobilization; for static dislocation, the major mechanisms involved in cold and warm forming include static pinning caused by the diffusion of interstitial solute atoms and static remobilization caused by thermally-activated dislocation climb and of junction dissociation.

- *Multiplication of mobile dislocations*

The dynamic generation of mobile dislocations is mainly contributed by, for example, Frank-Read source, cross-slip, and others [63]. When the material is under plastic loading, the generation rate of mobile dislocation can be considered to be proportional to the density of mobile dislocations and the mean free path [53]. Thus, the dynamic multiplication of mobile dislocation can be described as follows:

$$\frac{\partial \rho_{\mathrm{m}}^{\mathrm{gn}}}{\partial \varepsilon_{\mathrm{p}}} = M \lambda_{\mathrm{m}}^{\mathrm{gn}} \rho_{\mathrm{m}} \rho_{\mathrm{im}}^{-1/2} \tag{15}$$

where superscript 'gn' represents dislocation generation, the subscripts 'm' and 'im' refer to mobile and immobile dislocations, respectively; where $\partial \rho_{\mathrm{m}}^{\mathrm{gn}} / \partial \varepsilon_{\mathrm{p}}$ represents the generation rate of mobile dislocation density with respect to plastic strain (ε_{p}), *M* is Taylor factor, $\lambda_{\mathrm{m}}^{\mathrm{gn}}$ is the coefficient related to multiplication of mobile dislocations, ρ_{m} and ρ_{im} are densities of mobile and immobile dislocations, respectively.

- *Annihilation of mobile/immobile dislocations*

The annihilation of dislocations occurs in the case where a mobile/immobile dislocation meets a mobile dislocation with the opposite Burges vector. Based on the equation proposed by Ananthakrishna and Sahoo [64], the annihilation rates of mobile and immobile (cell and wall) dislocation densities can be represented by Eqs. (16) ~ (18), respectively.

$$\frac{\partial \rho_{\mathrm{m}}^{\mathrm{an}}}{\partial \varepsilon_{\mathrm{p}}} = M \lambda_{\mathrm{m,m}}^{\mathrm{an}} \rho_{\mathrm{m}} \rho_{\mathrm{m}} \tag{16}$$

$$\frac{\partial \rho_{\mathrm{im\text{-}cell}}^{\mathrm{an}}}{\partial \varepsilon_{\mathrm{p}}} = M \lambda_{\mathrm{m,im\text{-}cell}}^{\mathrm{an}} \rho_{\mathrm{m}} \rho_{\mathrm{im\text{-}cell}} \tag{17}$$

$$\frac{\partial \rho_{\mathrm{im\text{-}wall}}^{\mathrm{an}}}{\partial \varepsilon_{\mathrm{p}}} = M \lambda_{\mathrm{m,im\text{-}wall}}^{\mathrm{an}} \rho_{\mathrm{m}} \rho_{\mathrm{im\text{-}wall}} \tag{18}$$

where superscript ‘an’ represents annihilation, the subscripts ‘m’, ‘im-cell’ and ‘im-wall’ refer to mobile and cell immobile, and wall immobile dislocations, respectively; $\partial\rho_{\mathrm{m}}^{\mathrm{an}}/\partial\varepsilon_{\mathrm{p}}$, $\partial\rho_{\mathrm{im\text{-}cell}}^{\mathrm{an}}/\partial\varepsilon_{\mathrm{p}}$ and $\partial\rho_{\mathrm{im\text{-}wall}}^{\mathrm{an}}/\partial\varepsilon_{\mathrm{p}}$ are the annihilation rates dislocation densities with plastic strain (ε_{p}); $\lambda_{\mathrm{m,m}}^{\mathrm{an}}$, $\lambda_{\mathrm{m,im\text{-}cell}}^{\mathrm{an}}$, and $\lambda_{\mathrm{m,im\text{-}wall}}^{\mathrm{an}}$ are the coefficients related to the annihilation of the three types of dislocations, respectively.

- *Accumulation of immobile dislocations*

The dislocation accumulation process refers to the mobile dislocations immobilized by the immobile dislocations. During plastic deformation, the accumulation rate is considered to be proportional to the density of mobile dislocations and inversely proportional to the dislocation mean free path [51]. Hence, the dislocation accumulation rates can be obtained as follows:

$$\frac{\partial\rho_{\mathrm{im\text{-}cell}}^{\mathrm{ac}}}{\partial\varepsilon_{\mathrm{p}}}=M\lambda_{\mathrm{im\text{-}cell}}^{\mathrm{ac}}\rho_{\mathrm{m}}\rho_{\mathrm{im\text{-}cell}}^{1/2} \tag{19}$$

$$\frac{\partial\rho_{\mathrm{im\text{-}wall}}^{\mathrm{ac}}}{\partial\varepsilon_{\mathrm{p}}}=M\lambda_{\mathrm{im\text{-}wall}}^{\mathrm{ac}}\rho_{\mathrm{m}}\rho_{\mathrm{im\text{-}wall}}^{1/2} \tag{20}$$

where superscript ‘ac’ represents accumulation, the subscripts ‘m’, ‘im-cell’ and ‘im-wall’ refer to mobile and cell immobile, and wall immobile dislocations, respectively; $\partial\rho_{\mathrm{im\text{-}cell}}^{\mathrm{ac}}/\partial\varepsilon_{\mathrm{p}}$ and $\partial\rho_{\mathrm{im\text{-}wall}}^{\mathrm{ac}}/\partial\varepsilon_{\mathrm{p}}$ are the accumulation rates with plastic strain (ε_{p}); $\lambda_{\mathrm{im\text{-}cell}}^{\mathrm{ac}}$, $\lambda_{\mathrm{im\text{-}wall}}^{\mathrm{ac}}$ are coefficients related to the accumulation of the three types of dislocations, respectively.

- *Trapping of mobile dislocations*

When the mobile dislocations move into slipping systems, their mutual interactions could form dislocation junctions, and the density of dislocation junctions can be considered to be proportional to the density of mobile dislocations and inversely proportional mean free path [53]. The trapping rate of mobile dislocations can thus be written as:

$$\frac{\partial\rho_{\mathrm{m}}^{\mathrm{tr}}}{\partial\varepsilon_{\mathrm{p}}}=M\lambda_{\mathrm{m}}^{\mathrm{tr}}\rho_{\mathrm{m}}\bar{\Lambda} \tag{21}$$

where superscript ‘tr’ represents dislocation trapping, the subscripts ‘m’ refers to mobile dislocation; $\partial\rho_{\mathrm{m}}^{\mathrm{tr}}/\partial\varepsilon_{\mathrm{p}}$ is the dislocation trapping rate with plastic strain (ε_{p}); $\lambda_{\mathrm{m}}^{\mathrm{tr}}$ is the coefficient related to the dislocation trapping process.

Further, by replacing the mean free path term $\bar{\Lambda}$ in Eq (21) with Eq. (12) stated in Section 4.2.2, the trapping rate can be further designated by:

$$\frac{\partial\rho_{\mathrm{m}}^{\mathrm{tr}}}{\partial\varepsilon_{\mathrm{p}}}=M\lambda_{\mathrm{m}}^{\mathrm{tr}}\rho_{\mathrm{m}}^{3/2} \tag{22}$$

- *Nucleation of wall immobile dislocations*

With the continuous accumulation of cell immobile dislocations resulting in the dense concentration zone, higher critical external stress is needed to make cell immobile dislocation to be remobilized. The immobile dislocation pile-ups can become a stable state when they reach a critical condition. The formed stable pile-ups can create a strong local stress concentration to make some immobile dislocations in the cells become the nucleation of dislocation walls. According to reference [53], the dynamic nucleation rate can be denoted as:

$$\frac{\partial \rho_{\text{im-wall}}^{\text{nu}}}{\partial \varepsilon_{\text{p}}} = M \lambda_{\text{im-wall}}^{\text{nu}} \rho_{\text{im-cell}}^{3/2} \rho_{\text{m}} \tag{23}$$

where superscript 'nu' represents immobile dislocation nucleation, the subscripts 'm', 'im-cell' and 'im-wall' refer to mobile and cell immobile, and wall immobile dislocations, respectively; $\partial \rho_{\text{im-wall}}^{\text{nu}} / \partial \varepsilon_{\text{p}}$ is the nucleation rate of wall immobile dislocations with plastic strain (ε_{p}); $\lambda_{\text{im-wall}}^{\text{nu}}$ is the coefficient associated with this nucleation process.

- *Remobilization of immobile dislocations*

Some immobile dislocations can become mobile ones, which is also called the remobilization process when their densities reach a critical threshold [65]. For the wall and cell immobile dislocations, the remobilization rates can be formulated as:

$$\frac{\partial \rho_{\text{im-cell}}^{\text{rem}}}{\partial \varepsilon_{\text{p}}} = M \lambda_{\text{im-cell}}^{\text{rem}} \rho_{\text{im-cell}} \tag{24}$$

$$\frac{\partial \rho_{\text{im-wall}}^{\text{rem}}}{\partial \varepsilon_{\text{p}}} = M \lambda_{\text{im-wall}}^{\text{rem}} \rho_{\text{im-wall}} \tag{25}$$

where superscript 'rem' represents dislocation remobilization, the subscripts 'im-cell' and 'im-wall' refer to cell and wall immobile dislocations, respectively; $\partial \rho_{\text{im-cell}}^{\text{rem}} / \partial \varepsilon_{\text{p}}$ and $\partial \rho_{\text{im-wall}}^{\text{rem}} / \partial \varepsilon_{\text{p}}$ are the remobilization rates of cell and wall immobile dislocations with plastic strain (ε_{p}); $\lambda_{\text{im-cell}}^{\text{rem}}$, $\lambda_{\text{im-wall}}^{\text{rem}}$ are the coefficients associated with remobilization of the two types of dislocations, respectively.

- *Static pinning of mobile/immobile dislocations*

The cell dislocations could also be pinned and become immobile in the static state. This process is similar to dynamic pining but normally occurs at a low local strain rate and requires a long time to complete a pinning process. According to [53], the static pinning rate can be considered as proportional to the density of dislocation junctions, and the following equation is suggested to describe the rate with time, as given by:

$$\frac{\partial \rho_{\text{m}}^{\text{static-pin}}}{\partial t} = \lambda_{\text{m}}^{\text{static-pin}} \rho_{\text{m}}^{3/2} \tag{26}$$

$$\frac{\partial \rho_{\text{im-cell}}^{\text{static-pin}}}{\partial t} = \lambda_{\text{im-cell}}^{\text{static-pin}} \rho_{\text{im-cell}}^{3/2} \tag{27}$$

where superscript 'static-pin' represents static pinning of dislocations, and the subscripts 'm' and 'im-cell' refer to mobile and cell immobile dislocations, respectively; $\partial \rho_{\text{m}}^{\text{static-pin}} / \partial t$ and $\partial \rho_{\text{im-cell}}^{\text{static-pin}} / \partial t$ are the pinning rates of the two types of dislocations with time (*t*), respectively;

$\lambda_{\text{im-cell}}^{\text{static-pin}}$, $\lambda_{\text{im-wall}}^{\text{static-pin}}$ are the coefficients for static pinning of the two types of dislocations, respectively.

- *Static remobilization of immobile dislocations*

Both cell and wall immobile dislocations can be remobilized in a static state on the condition that dislocation behaviors of climb and dissociation were thermally activated. It is reported that the dislocation remobilization rates with time at a static state present a proportional change to their densities, as given by [53]:

$$\frac{\partial \rho_{\text{im-cell}}^{\text{static-rem}}}{\partial t} = \lambda_{\text{im-cell}}^{\text{static-rem}} \rho_{\text{im-cell}} \tag{28}$$

$$\frac{\partial \rho_{\text{im-wall}}^{\text{static-rem}}}{\partial t} = \lambda_{\text{im-wall}}^{\text{static-rem}} \rho_{\text{im-wall}} \tag{29}$$

where superscript ‘static-rem’ represents static remobilization of dislocations, and the subscripts ‘im-cell’ and ‘im-wall’ refer to cell and wall immobile dislocations, respectively; $\partial \rho_{\text{im-cell}}^{\text{static-rem}} / \partial t$ and $\partial \rho_{\text{im-wall}}^{\text{static-rem}} / \partial t$ are the pinning rates of the two types of dislocations with time (t), respectively; $\lambda_{\text{im-cell}}^{\text{static-rem}}$, $\lambda_{\text{im-wall}}^{\text{static-rem}}$ are the coefficients related to the two types of dislocations, respectively.

4.3.2 Strain-dependent evolution of mobile dislocation density

The evolution of dislocation densities of the material during plastic deformation is a result of contributions made by different dislocation behaviors associated with the different types of dislocations. As described in Section 4.3.1, some dislocation behaviors can contribute to an increase in the densities, and some also contribute to a decrease in the densities.

For the dynamic evolution of mobile dislocation density with plastic strain, the multiplication of mobile dislocations (as given in Eq. (15)), and remobilization of immobile dislocations (as given in Eqs. (24) and (25)), contribute to an increase in the density. Thus, by combining Eqs. (15), (24), and (25), the ‘positive’ component ($\partial \rho_{\text{m}}^{+} / \partial \varepsilon_{\text{p}}$) for mobile dislocation density evolution can be calculated by:

$$\frac{\partial \rho_{\text{m}}^{+}}{\partial \varepsilon_{\text{p}}} = \frac{\partial \rho_{\text{m}}^{\text{gn}}}{\partial \varepsilon_{\text{p}}} + \frac{\partial \rho_{\text{im,cell}}^{\text{re}}}{\partial \varepsilon_{\text{p}}} + \frac{\partial \rho_{\text{im,wall}}^{\text{re}}}{\partial \varepsilon_{\text{p}}} \tag{30}$$

Likewise, the annihilation of mobile dislocations (as given in Eq. (16)), accumulation of immobile dislocations (as given in Eqs. (19) and (20)), and trapping of mobile dislocations (as given in Eq. (21)), contribute to a decrease in the density. Thus, by combining Eq. (16), (19), and (20), the ‘negative’ component ($\partial \rho_{\text{m}}^{-} / \partial \varepsilon_{\text{p}}$) for mobile dislocation density evolution can be calculated by:

$$\frac{\partial \rho_{\text{m}}^{-}}{\partial \varepsilon_{\text{p}}} = 2\frac{\partial \rho_{\text{m}}^{\text{an}}}{\partial \varepsilon_{\text{p}}} + \frac{\partial \rho_{\text{im,cell}}^{\text{an}}}{\partial \varepsilon_{\text{p}}} + \frac{\partial \rho_{\text{im,wall}}^{\text{an}}}{\partial \varepsilon_{\text{p}}} + \frac{\partial \rho_{\text{im,cell}}^{\text{ac}}}{\partial \varepsilon_{\text{p}}} + \frac{\partial \rho_{\text{im,wall}}^{\text{ac}}}{\partial \varepsilon_{\text{p}}} + \frac{\partial \rho_{\text{m}}^{\text{tr}}}{\partial \varepsilon_{\text{p}}} \tag{31}$$

Consequently, by summing the 'positive' component ($\partial\rho_{\mathrm{m}}^{+}/\partial\varepsilon_{\mathrm{p}}$) given in Eq. (30) and the 'negative' component ($\partial\rho_{\mathrm{m}}^{-}/\partial\varepsilon_{\mathrm{p}}$) given in Eq. (31), the dynamic evolution of mobile dislocation density can be obtained:

$$\frac{\partial\rho_{\mathrm{m}}^{\mathrm{dynamic}}}{\partial\varepsilon_{\mathrm{p}}}=\frac{\partial\rho_{\mathrm{m}}^{+}}{\partial\varepsilon_{\mathrm{p}}}-\frac{\partial\rho_{\mathrm{m}}^{-}}{\partial\varepsilon_{\mathrm{p}}} \tag{32}$$

For the static evolution of mobile dislocation density with time, as discussed in Section 4.3.1, the static remobilization of cell and wall immobile dislocations contributes to an increase in the density, as given by Eqs. (28) and (29); however, the static pinning of mobile dislocation contributes to a decrease in the density, as given in Eq. (26). Hence, the static evolution equation can be calculated by summing the 'positive' ($\partial\rho_{\mathrm{m}}^{+}/\partial t$) and 'negative' ($\partial\rho_{\mathrm{m}}^{-}/\partial t$) contributors, represented by:

$$\frac{\partial\rho_{\mathrm{m}}^{\mathrm{static}}}{\partial t}=\frac{\partial\rho_{\mathrm{m}}^{+}}{\partial t}-\frac{\partial\rho_{\mathrm{m}}^{-}}{\partial t}=\left(\frac{\partial\rho_{\mathrm{im\text{-}cell}}^{\mathrm{static\text{-}rem}}}{\partial t}+\frac{\partial\rho_{\mathrm{im\text{-}wall}}^{\mathrm{static\text{-}rem}}}{\partial t}\right)-\left(\frac{\partial\rho_{\mathrm{m}}^{\mathrm{static\text{-}pin}}}{\partial t}\right) \tag{33}$$

4.3.3 Strain-dependent evolution of immobile dislocation density

Similar to Section 4.3.2, the 'positive' and 'negative' contributors are used to analyze the immobile dislocation density evaluation. For the dynamic evolution of cell immobile dislocation density, the trapping of mobile dislocations (as given in Eq. (22)) and the accumulation of cell immobile dislocations (as given in Eq. (19)), contribute to an increase in the cell dislocation density, which makes the 'positive' contributor ($\partial\rho_{\mathrm{im\text{-}cell}}^{+}/\partial\varepsilon_{\mathrm{p}}$). The annihilation and remobilization of wall immobile dislocation (as given in Eq. (18) and (20)), and the nucleation of wall immobile dislocations (as given in Eq. (23)), contribute to a decrease in the density, which makes the 'positive' contributor ($\partial\rho_{\mathrm{im\text{-}cell}}^{-}/\partial\varepsilon_{\mathrm{p}}$). Hence, by combining Eqs. (18)-(20), (22), and (23), the equation for determining the dynamic evolution of cell immobile dislocation density can be obtained:

$$\frac{\partial\rho_{\mathrm{im\text{-}cell}}^{\mathrm{dynamic}}}{\partial\varepsilon_{\mathrm{p}}}=\frac{\partial\rho_{\mathrm{im\text{-}cell}}^{+}}{\partial\varepsilon_{\mathrm{p}}}-\frac{\partial\rho_{\mathrm{im\text{-}cell}}^{-}}{\partial\varepsilon_{\mathrm{p}}}=\left(\frac{\partial\rho_{\mathrm{im\text{-}cell}}^{\mathrm{tr}}}{\partial\varepsilon_{\mathrm{p}}}+\frac{\partial\rho_{\mathrm{im\text{-}wall}}^{\mathrm{ac}}}{\partial\varepsilon_{\mathrm{p}}}\right)-\left(\frac{\partial\rho_{\mathrm{im\text{-}cell}}^{\mathrm{an}}}{\partial\varepsilon_{\mathrm{p}}}+\frac{\partial\rho_{\mathrm{im\text{-}cell}}^{\mathrm{rem}}}{\partial\varepsilon_{\mathrm{p}}}+\frac{\partial\rho_{\mathrm{im\text{-}wall}}^{\mathrm{nu}}}{\partial\varepsilon_{\mathrm{p}}}\right) \tag{34}$$

For the static evolution of cell immobile dislocation density, the static pinning of mobile dislocations contributes to increasing the density (as given in Eq. (26)), and the static remobilization and static pinning of cell immobile dislocations (as given in Eqs. (27) and (28)). Thus, by combining Eqs. (26)-(28), the static evolution equation for cell immobile dislocation density can be obtained:

$$\frac{\partial\rho_{\mathrm{im\text{-}cell}}^{\mathrm{static}}}{\partial t}=\frac{\partial\rho_{\mathrm{im\text{-}cell}}^{+}}{\partial t}-\frac{\partial\rho_{\mathrm{im\text{-}cell}}^{-}}{\partial t}=\frac{\partial\rho_{\mathrm{m}}^{\mathrm{static\text{-}pin}}}{\partial t}-\left(\frac{\partial\rho_{\mathrm{im\text{-}cell}}^{\mathrm{static\text{-}rem}}}{\partial t}+\frac{\partial\rho_{\mathrm{im\text{-}cell}}^{\mathrm{static\text{-}pin}}}{\partial t}\right) \tag{35}$$

For the dynamic evolution of wall immobile dislocation density, the 'positive' contributor ($\partial\rho_{\mathrm{im\text{-}wall}}^{+}/\partial\varepsilon_{\mathrm{p}}$) is composed of the nucleation and accumulation of wall dislocations (as given in Eq. (23) and (20)), and the 'negative' contributor ($\partial\rho_{\text{im-wall}}^{-}/\partial\varepsilon_{\text{p}}$) contains the annihilation and remobilization of wall dislocations (as given in Eq. (18) and (25)). Hence, combining Eqs. (18), (20), (23), and (25) can lead to the governing equation for the dynamic evolution of wall immobile dislocation density, as denoted by:

$$\frac{\partial\rho_{\text{im-wall}}^{\text{dynamic}}}{\partial\varepsilon_{\text{p}}}=\frac{\partial\rho_{\text{im-wall}}^{+}}{\partial\varepsilon_{\text{p}}}-\frac{\partial\rho_{\text{im-wall}}^{-}}{\partial\varepsilon_{\text{p}}}=\left(\frac{\partial\rho_{\text{im-wall}}^{\text{nu}}}{\partial\varepsilon_{\text{p}}}+\frac{\partial\rho_{\text{im-wall}}^{\text{ac}}}{\partial\varepsilon_{\text{p}}}\right)-\left(\frac{\partial\rho_{\text{im-wall}}^{\text{an}}}{\partial\varepsilon_{\text{p}}}+\frac{\partial\rho_{\text{im-wall}}^{\text{rem}}}{\partial\varepsilon_{\text{p}}}\right) \tag{36}$$

For the static evolution of wall immobile dislocation density, the static pinning of cell immobile dislocation (as given in Eq. (27)) makes the 'positive' contributor ($\partial\rho_{\text{im-wall}}^{+}/\partial t$), and the static remobilization (as given in Eq. (29)) of wall dislocations makes the 'negative' contributor ($\partial\rho_{\text{im-wall}}^{-}/\partial t$). Hence, by combining Eqs. (27) and (29) (20), the static evolution of wall immobile dislocation density can be formulated as follows:

$$\frac{\partial\rho_{\text{im-wall}}^{\text{static}}}{\partial t}=\frac{\partial\rho_{\text{im-wall}}^{+}}{\partial t}-\frac{\partial\rho_{\text{im-wall}}^{-}}{\partial t}=\frac{\partial\rho_{\text{im-cell}}^{\text{static-pin}}}{\partial t}-\frac{\partial\rho_{\text{im-wall}}^{\text{static-rem}}}{\partial t} \tag{37}$$

4.3.4 Temperature-dependent evolution of dislocation densities

According to whether it is thermally activated or not, dislocation behaviors are classified as temperature-dependent and temperature-independent processes. Among the dislocation behaviors described in Section 4.3.1, except for the generation of mobile dislocations and accumulation of immobile dislocations, other dislocation behaviors are sensitive to temperature as well the strain rate [53]. Regarding the temperature-/rate-dependence in material modeling, it is still a challenging issue as thermally-related dislocation behaviors are overly intricate with more complex mechanisms involved. To seek an efficient description, a power law was proposed by Motaman et al. [53] to capture the sensitivities of temperature and rate in constitutive modeling. In this work, a similar semi-physically function was employed to link the temperature and rate dependence on the dislocation behaviors. First, the temperature dependence is constructed as follows:

$$\left(\lambda_i-\lambda_i^{\text{ref-temp}}\right)/\lambda_i^{\text{ref-temp}}=\omega_i\left[\left(T-T_{\text{ref}}\right)/T_{\text{ref}}\right]^{r_i} \tag{38}$$

where *T* is temperature, *T*$_0$ is the reference temperature in the given range, λ_i and $\lambda_i^{\text{ref-temp}}$ are the material coefficients at the current and reference temperatures, respectively, ω_i and r_i are newly defined parameters associating the temperature sensitivity and changing rate, respectively. It should be stressed that the reference temperature can be defined as an arbitrary value between the targeted temperature range. In this work, it is assumed as the lower limit of the temperature range, namely, the room temperature.

Second, Eq. (39) is introduced to describe the strain rate dependence on the probability change of dislocation behavior induced by strain rate variation in the following [53]:

$$\lambda_i/\lambda_i^{\text{ref-strain rate}}=\beta_i\left(\dot{\varepsilon}_{\text{p}}/\dot{\varepsilon}_{\text{ref}}\right)^{s_i} \tag{39}$$

where $\dot{\varepsilon}_{\text{ref}}$ is the reference strain rate in the given range of strain rate, $\lambda_i^{\text{ref-strain rate}}$ are the material coefficients at reference strain rate, β_i and s_i are newly defined parameters associated with strain rate sensitivity, respectively. Similarly, $\lambda_i^{\text{ref-strain rate}}$ is set as the lower limit value of the given strain rate range. In the modeling process, two reference values of the material coefficients will induce convenience in derivation and numerical implementation of the equations. Thus, a unified reference coefficient (λ_i^{ref}) can be defined at the lower limit in the range of the temperatures and strain rates in the following:

$$\lambda_i^{\text{ref}} = \lambda_i^{\text{ref-temp}}\Big|_{\substack{\text{minimum}\\ \text{strain rate}}} = \lambda_i^{\text{ref-strain rate}}\Big|_{\substack{\text{minimum}\\ \text{temperature}}} \tag{40}$$

Then, the above Eqs. (38) and (39) can be re-formulated as:

$$\begin{cases} \left(\lambda_i - \lambda_i^{\text{ref}}\right)/\lambda_i^{\text{ref}} = \omega_i\left[\left(T - T_{\text{ref}}\right)/T_{\text{ref}}\right]^{r_i} \\ \lambda_i/\lambda_i^{\text{ref}} = \beta_i\left(\dot{\varepsilon}_{\text{p}}/\dot{\varepsilon}_{\text{ref}}\right)^{s_i} \end{cases} \tag{41}$$

By using the normalization method, Eq. (41) can be simplified as:

$$\begin{cases} \hat{\lambda}_i = 1 + \omega_i\left(\hat{T} - 1\right)^{r_i} \\ \hat{\lambda}_i = \beta_i\left(\hat{\dot{\varepsilon}}_{\text{p}}\right)^{s_i} \end{cases} \tag{42}$$

Hence, the temperature- and rate-related dependencies can be coupled into one power-form equation as given by:

$$\hat{\lambda}_i = \left[1 + \omega_i\left(\hat{T} - 1\right)^{r_i}\right] \cdot \beta_i\left(\hat{\dot{\varepsilon}}_{\text{p}}\right)^{s_i} \tag{43}$$

As aforementioned, dislocation generation and accumulation are temperature-independent so that their corresponding values of ω_i and r_i are set as zero. Likewise, for the strain rate-related dependence, besides the two kinds of temperature-independent dislocation behaviors, the two kinds of static dislocation processes, namely, static pinning and static remobilization are strain rate independent. Thus, their corresponding values for β_i and s_i are set as zero.

Table 2 The possible range of the coefficient of different dislocation behaviors.

Dislocation behaviors	Temperature dependence			Strain rate dependence		
	Effect	ω_i	r_i	Effect	β_i	s_i
Generation of mobile dislocations	/	0	0	/	0	0
Annihilation of mobile/immobile dislocations	↑	+	+	↓	+	-
Accumulation of immobile dislocations	/	0	0	/	0	0
Trapping of mobile dislocations	↑	+	+	↓	+	-
Nucleation of wall dislocations	↑ or ↓	/	+	↑ or ↓	/	/
Remobilization of immobile dislocations	↑	+	+	↑ or ↓	/	/
Static pinning of mobile/immobile dislocations	↑	+	+	/	0	0
Static remobilization of immobile dislocations	↑	+	+	/	0	0

The possible ranges of parameter values are shown in Table 2. It should be noted that the upward and downward arrows mean that the parameter has “positive” and “negative” effects, respectively, on the dislocation behavior. Accordingly, the notations ‘+’ and ‘-’ indicate that the parameters have positive and negative value ranges, respectively.

5. Discussion

5.1. Calibration and validation

5.1.1. Parameters configuration

Parameter configuration is an important procedure for ensuring the validity and wide application of different constitutive models. In the proposed model, some physically-based internal-state variables can hardly be experimentally and microscopically characterized. Optimization-based inverse methods could provide accurate and efficient identification of parameters for such kinds of physically-based models [66]. Thus, in this work, the optimization method based on a combination of the hypothesis of physics nature as well as the feasible experiments are used for parameter identification. In tandem with this, three aspects of crucial problems need to be addressed. One is how to construct a multi-objective function to comprehensively cover the temperature-dependent plastic flow stress and the nonlinear unloading with plastic strain accumulation. The second is how to numerically solve complex differential equations involved in the CDD model since they cannot be explicitly calculated. The last is how to establish an effective and robust optimization way to ensure that the parameter is accurately determined, and the calculation is well converged.

As unloading occurs when the whole loading process is completed, the accurate modeling of the unloading nonlinearity should be achieved on the condition that the stress-strain response upon loading is effectively described. To realize this purpose, two optimization objectives are considered, i.e., the temperature-dependent stress-strain response upon loading and the temperature-dependent nonlinear elastic strain upon unloading.

The first one is represented by the true stress-strain curve determined by the isothermal uniaxial tension experiments. It should be mentioned that the experimental curve used for optimization is fitted by the Swift function considering the lower strain level of ultimate strength and the limited elongation of high strength Ti-3Al-2.5V alloy. The error function is defined as:

$$\mathcal{E}_{\text{flow stress}}\left(\boldsymbol{C}\right)=\frac{1}{P_1}\sum_{i=1}^{M}\frac{1}{Q_1}\sum_{j=0}^{N}\left|\frac{\sigma_{ij}^{\text{pred}}\left(\boldsymbol{C},T_i,\varepsilon_{\text{p}}^{j}\right)}{\sigma_{ij}^{\text{exp}}\left(T_i,\varepsilon_{\text{p}}^{j}\right)}-1\right| \tag{44}$$

where ***C*** is the model’s coefficient matrix. P_1 is the total number of experiments for calibration performed at various temperatures with a reference rate. Q_1 is the total number of discrete stress-strain data points at a given temperature. T_i is the temperature condition of the calibration experiment. $\varepsilon_{\text{p}}^{j}$ is the discrete plastic strain point that can be calculated from

$\varepsilon_{\mathrm{p}}^{j} = j\Delta\varepsilon_{\mathrm{p}}$ ($\Delta\varepsilon_{\mathrm{p}}$ is the interval between the neighboring plastic strain points and $j \in [0, N]$ is the sequence number of the strain point). $\sigma_{ij}^{\mathrm{pred}}$ is the flow stress predicted within the model at temperature T_i , and the strain points $\varepsilon_{\mathrm{p}}^{j}$. $\sigma_{ij}^{\mathrm{exp}}$ is the flow stress in isothermal tension experiments at temperature T_i and strain points $\varepsilon_{\mathrm{p}}^{j}$.

Likewise, the other objective in optimization is the nonlinear elastic strain, which is constructed as follows:

$$\tilde{e}_{\text{non-e}}(\boldsymbol{C}) = \frac{1}{P_2}\sum_{i=1}^{P}\frac{1}{Q_2}\sum_{j=0}^{Q}\left|\frac{\varepsilon_{\text{transient, } ij}^{\text{non-e, pred}}\left(\boldsymbol{C}, T_i, \varepsilon_{\mathrm{p}}^{j}\right)}{\varepsilon_{\text{transient, } ij}^{\text{non-e, exp}}\left(T_i, \varepsilon_{\mathrm{p}}^{j}\right)} - 1\right| \tag{45}$$

where P_2 is the total number of calibration loading-unloading-reloading experiments at different temperatures with a reference strain rate. Q_2 is the total number of the discrete data points of plastic strain-nonlinear elastic strain at a given temperature. The experimental results of nonlinear elastic strain *vs.* plastic strain at various temperatures are also used in optimization for improving global accuracy.

The final objective function is thus constructed as a sum of the above two components, as denoted as follows:

$$Error(\boldsymbol{C}) = \tilde{e}_{\text{flow stress}}(\boldsymbol{C}) + \tilde{e}_{\text{non-e}}(\boldsymbol{C}) \tag{46}$$

By minimizing the final error, the parameters involved in the CDD-based modeling framework can thus be determined.

As many coefficients are introduced in the constitutive model to model different dislocation behaviors in loading and unloading, finding a global solution to this multi-objective optimization problem is quite important. In this research, the "GlobalSearch" optimization method is employed in combination with GA (genetic algorithm) which is coded by using the MATLAB script. A detailed description of the numerical implementation process and algorithm is stated in Appendix B.

5.1.2. Assessment of the model

Using the above-constructed parameter configuration method, the parameters of the CDD-based constitutive model can be determined based on the experimental results described in Section 2. For Ti-3Al-2.5V alloy, the Burger's vector is 2.95×10^{-10} meter and the Taylor factor can be set as 5 [67]. The lowest temperature of 293 K in the temperature range of [20, 100, 200, 300, 400] °C is defined as the reference value. As the unloading nonlinearity is not sensitive to strain rate, a constant rate of 0.001 s^{-1} is used, and there is no need to define the reference strain rate. The mean relative error can be minimized to 4.71% after 393 iterations. The dislocation behaviors related coefficients are shown in Table C1 shown in Appendix C, while the physical material constants and reference coefficients are shown in Table C2 shown in Appendix C. The model coefficients related to temperature dependence are shown in Table C3 shown in Appendix C.

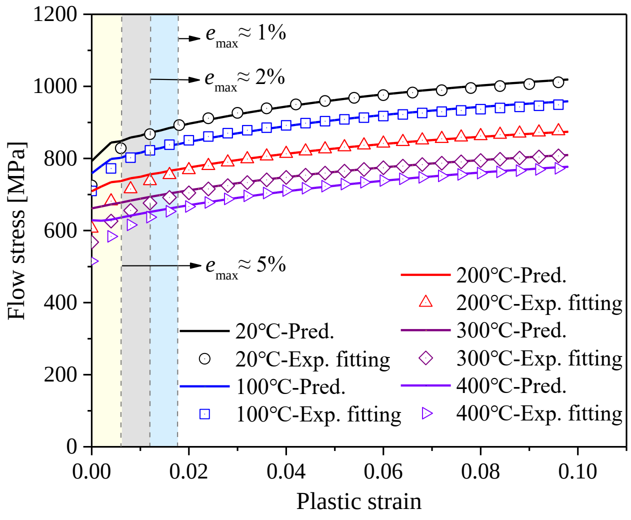

Fig. 15. Flow stress predicted by CDD-based model.

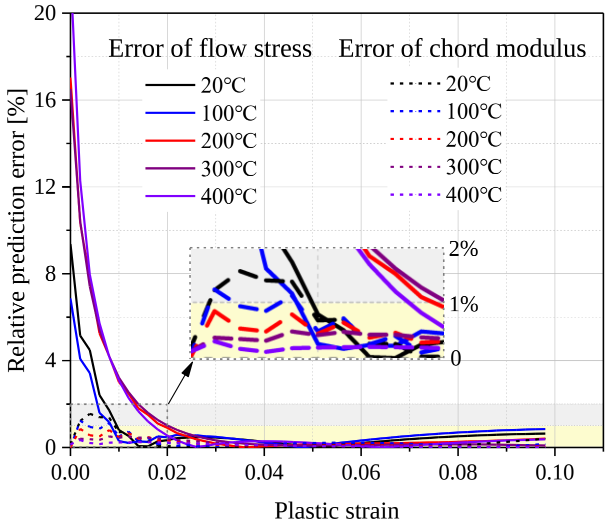

Fig. 16. Analysis of prediction errors of CDD-based model.

Both the uniaxial tension tests and tension loading-unloading-reloading tests at different temperatures are used to validate the CDD-based model. Fig. 15 compares the experimental flow stress curves and the predicted ones with the CDD model. It can be found that the predicted curves can well agree with the experiment fitting curves except for the very narrow range in the initial plastic loading stage. As shown in Fig. 16, at the beginning of plastic deformation, the prediction error is less than 9.3% within 100℃, and then presents an increasing trend at the higher temperature. With the increase of the plastic strain, the maximum error of the flow stress at the five temperatures can be reduced to about 5% at the plastic strain of 0.06 and can be further reduced to about 2% at 0.012. When the plastic strain exceeds 0.018, the maximum error is below about 1%.

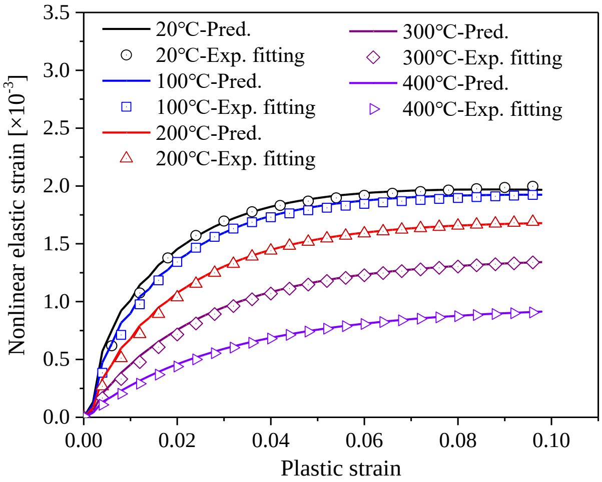

Fig. 17. Nonlinear elastic strain predicted by the model.

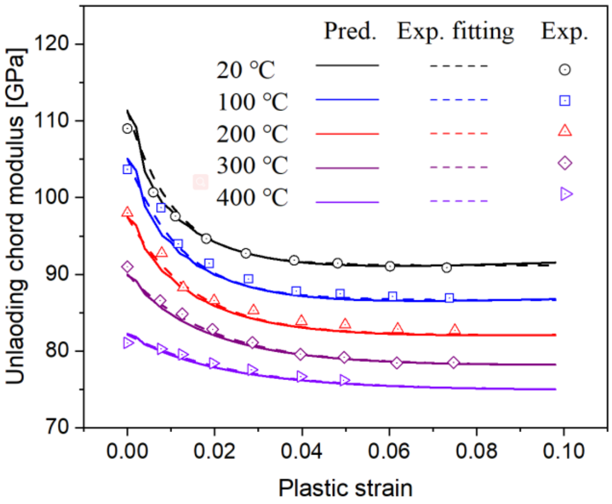

Fig. 18. Unloading chord modulus predicted by the model.

Recalling the statement in Section 3 that the total recovery strain contains the pure elastic strain component and the nonlinear elastic strain component. Through the model established in Section 4, the nonlinear elastic strain components at different plastic strain levels and temperatures can be calculated. Fig. 17 compares the prediction results by the model and the experimental ones. It is found that the model can well predict the changing trends of the nonlinear elastic strain with plastic strain at different temperatures. Besides, the nonlinear elastic strain directly contributes to the degradation effect of elastic modulus. As shown in Fig. 18, the unloading chord moduli calculated by the model are compared with the experimentally fitted unloading moduli and the original experimental points, showing that the predicted results are well agree with the experimental results. Furthermore, it is found in Fig. 16 that the maximum prediction error between the prediction and the experimental fitting moduli is about 1.5%. The error is can be reduced to less than 0.5% when the plastic strain is more than about 0.013. Therefore, from the perspectives of both flow stress and unloading chord modulus, the model can be effectively predictive.

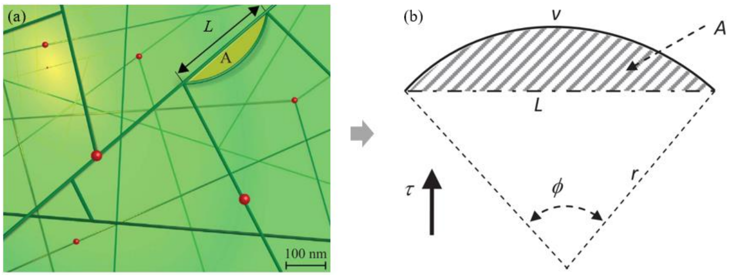

Fig. 19. Dislocation-based explanation for nonlinear unloading: (a) Schematic of the pinned dislocation structures [68]; (b) Schematic of the reversible shear strain under loading [28].

5.2. Mechanisms of nonlinear unloading under thermal-mechanical loading

As discussed previously, the reversible movement of mobile dislocations contributes to the nonlinear elastic strain. Fig. 19 (a) schematically illustrates the dislocation structures that are impeded by the pinning obstacles such as grain boundaries, sub-cells, and solute particles, or dislocations piled ups around grain boundaries. During plastic deformation, the dislocation segments with their ends fixed will be bowed out under external forces. For those segments without sufficient shear stress applied (under critical shear stress), they can not become dislocation sources and keeps in a bow-out state [59]. However, when the external forces are unloaded, these reversible dislocation segments can move to a new equilibrium with the relaxation of the stress and thus contribute to nonlinear elastic strain during loading [38,55,56,69]. As illustrated in Eq. (9), the density of the reversible mobile dislocations in the deformed material prior to unloading as well as the mean free path of dislocations determines the amount of the nonlinear elastic strain that can be accumulated during unloading. Thus, how the reversible mobile dislocation density and the mean free path develop under the thermal-mechanical working can be related to the nonlinear unloading behavior. For this purpose, based on the proposed model, the evolutions of various dislocation densities with plastic strain at different forming temperatures are discussed as follows.

Fig. 20 (a) shows the evolution of total mobile dislocation density with plastic strain under different temperatures. The curves under the five sets of temperatures present a similar trend。 Overall, increasing the plastic strain, the total mobile dislocation density quickly increased at a very high level at the beginning of plastic deformation and then presents a slight decrease to a gradually flat state as the plastic deformation continues. With increasing the deformation temperature, the overall dislocation density is reduced, and a higher temperature makes a higher reduction rate as well as weakened variation of density along with plastic strain. The overall trend of dislocation evolution with both plastic strain and temperature is similar to the results reported in [61].

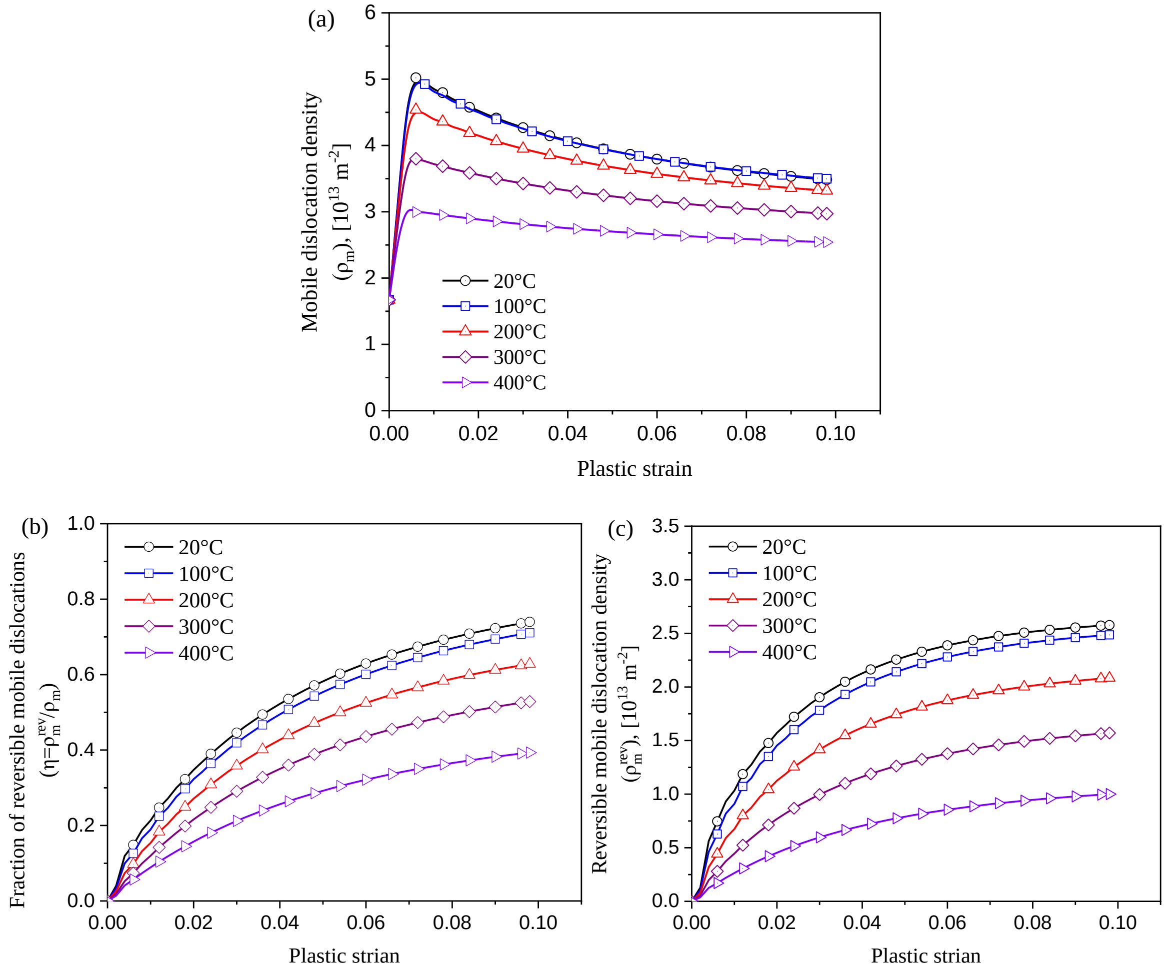

Fig. 20. Evolution of the mobile dislocation density at different temperatures: (a) the total mobile dislocations; (b) the fraction of reversible dislocations to total mobile dislocations; (c) the reversible mobile dislocations.

Among the mobile dislocations, only part of them be reversible and contribute to creating the nonlinear elastic strain. Fig. 20 (b) demonstrates the dynamic fraction of reversible ones from the total mobile dislocations with the accumulation of plastic strain. It can be observed that the percentage of reversible dislocations gradually increases at a decayed date as the plastic strain increases. This fraction is very sensitive to the deformation temperature. With the increase in temperature, the fraction of reversible mobile dislocation is decreased accordingly, and the thermal effect on the reduction of this fraction is aggravated at higher temperatures. At the strain level of 0.1, the fraction of reversible dislocation under cold deformation is about twice as compared to warm deformation at 400 °C. As defined in Eq. (8), by multiplying the fraction and the total mobile dislocation density, the dynamic evolution of reversible mobile dislocation density can be obtained, as illustrated in Fig. 20 (c). It can be observed from Fig. 20 (c) that the reversible mobile dislocation density increases at an exponential saturation trend with plastic strain, which indicates that the density increases at a relatively high rate under a low strain level and then continues but at a decaying rate. When it comes to temperature dependence, it can be observed from Fig. 20 (c) that the saturated density is significantly sensitive to the deformation temperature. At the strain level of 0.1, the density of reversible dislocations under cold deformation is about 2.5 times higher than that under warm deformation at 400 °C. As described in Eq. (9), the nonlinear elastic strain is proportional to the density of reversible dislocations. This is why the nonlinear elastic strain (as shown in Fig. 14) under 400 °C is much smaller than that under cold deformation. In addition, it also can be found from Fig. 20 (c) that the reversible dislocation density is more sensitive to high temperatures. At higher temperatures, the increasing rate of dislocation density is decreased, and the saturated dislocation density is remarkably decreased, resulting in the experimental phenomena of temperature-dependent nonlinear unloading.

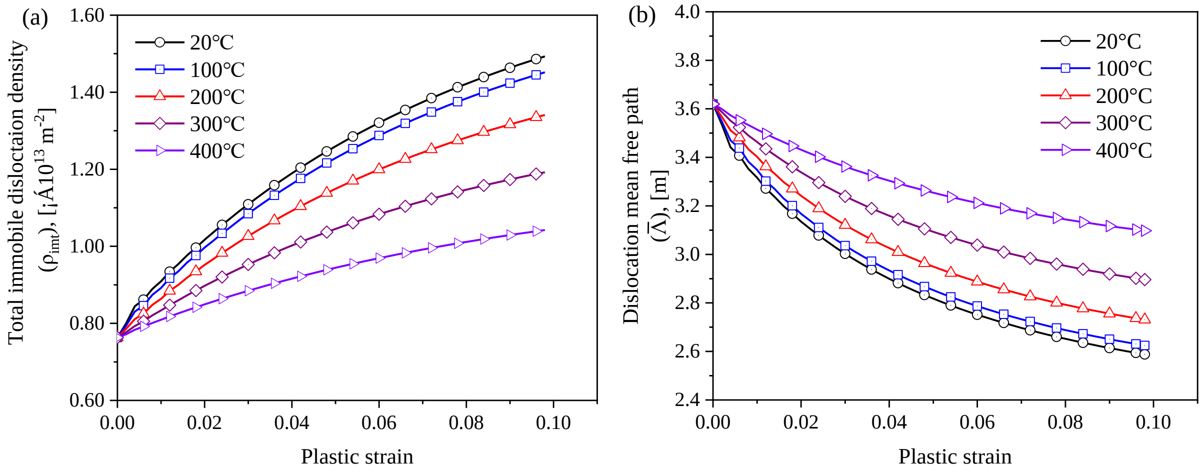

Fig. 21. Evolution of immobile dislocation density and mean free path at different temperatures: (a) total immobile dislocation density; (b) dislocation mean free path.

As discussed in Section 4.1, another factor affecting the nonlinear elastic strain is dislocation mean free path, which is related to the density of immobile dislocations. By using the developed model, the evolution of the immobile dislocation density along with plastic deformation at different temperatures can be calculated, as shown in Fig. 21 (a). As can be observed in this figure, the density of total immobile dislocations presents an increasing trend as the plastic strain increases. In addition, deformation temperature has a significant influence on the immobile dislocation density in the deformed material. Similar to the mobile dislocation evolution, with the increase in temperature, the immobile dislocation density is decreased also, and the decrease in density is much more pronounced at higher plastic strain levels relatively. As described in Section 4.2.2, the mean free path of dislocation can be considered to be proportional to the average spacing distance and can be represented by Eq. (12) through the immobile dislocation density. By using this equation, the mean free path can be calculated, as illustrated in Fig. 21 (b). It can be observed from Fig. 21 (b) that the mean free path presents a decaying trend as the plastic strain increases. As the mean free path is related to immobile dislocation density, it is also very sensitive to temperature. The temperature sensitivity presents a reverse trend with the increase of the dislocation densities. At high temperatures within the warm domain in this study, the mean free path becomes less sensitive to the temperature.

In summary, the degradation evolution of unloading chord modulus with plastic deformation is a result of the superposition of pure elastic strain and nonlinear elastic strain. As described in Eq. (9), the nonlinear elastic strain is jointly determined by the density of reversible mobile dislocations and the dislocation mean free path. The density of reversible mobile dislocations, however, is affected by the total dislocations in the deformed material including mobile and immobile. By using the proposed model, the fraction of reversible mobile dislocation density is extracted to characterize the coupled effect. During the plastic deformation process, increasing the possibility of creating plastic strain makes the fraction of reversible mobile dislocations increase; however, the increase in immobile dislocation density presents a negative effect on the fraction of the reversible mobile dislocations. The two aspects jointly make the reversible mobile dislocation density increase at a rapid rate with plastic strain, as shown in Fig. 20 (c). At the same time, the evolution of immobile dislocation makes the dislocation mean free path decrease at a relatively slower rate with plastic strain, as shown in Fig. 21 (b). The rapidly increased reversible mobile dislocation density and the slowly decreased mean free path make the nonlinear elastic strain change with plastic strain at an exponential saturated growth trend as experimentally observed (shown in Fig. 14). Such a change of nonlinear elastic strain further results in the exponential decaying change in chord modulus with plastic strain as experimentally observed (shown in Fig. 12). With the increase of deformation temperature, the thermally-activated dislocation interactions lead to the temperature-dependent evolution behaviors of the reversible mobile dislocation density and dislocation mean free path (shown in Fig. 20 (c) and 21 (b)). This further makes the increments of nonlinear elastic strain with plastic strain smaller under higher deformation temperatures (shown in Fig. 14). Hence, when the temperature is increased, the nonlinear elastic strain is reduced, thus resulting in a weakened nonlinearity of strain-related chord modulus degradation as experimentally observed (shown in Fig. 12).

6. Conclusions

In this research, the nonlinear unloading behavior within cold and warm deformation domains is experimentally investigated by using a near-alpha high-strength titanium alloy. A physically-based model considering the reversible mobile dislocations is developed to reproduce the thermal-mechanical affected degradation of elastic modulus. Based on the modeling combined with experiments, the dislocation-dominated mechanism is discussed for a better understanding of unloading behavior in thermal-mechanical working. The main conclusions are summarized as follows:

- The nonlinear unloading behavior in thermal-mechanical working within cold and warm domains is clarified. The unloading chord modulus under cold deformation is degraded dramatically at a low plastic strain level and then gradually gets a saturated state. Increasing the temperature up to 400 ℃, the strain-related degradation of chord modulus drops to about one-third as compared to cold deformation, and the degradation rate is weakened simultaneously. Regarding the nonlinearity of the unloading stress-strain curve, it increases with plastic strain and gradually trends to be saturated; simultaneously, this nonlinearity is significantly weakened in high-temperature deformation conditions.
- From the view of dislocation interactions upon loading/unloading, the reversible mobile dislocation is modeled to describe the partial mobile dislocations that contribute to unloading nonlinearity. By concurrently considering the various mobile and immobile dislocation behaviors, a physically-based model is established for the prediction of material response during loading as well as the strain- and temperature-dependent evolution modulus degradation effect in thermal-mechanical working. The model is experimentally assessed, showing good capability for analyzing the chord modulus reduction behavior.
- With the accumulation of plastic strain, the rapidly increased reversible mobile dislocation density and the slowly decreased mean free path make the nonlinear elastic strain change, leading to an exponential decaying of chord modulus. With the increase in deformation temperature, the thermally-activated dislocation behaviors lead to the temperature-dependent evolutions of the reversible dislocation density and mean free path, which affects makes the increments of nonlinear elastic strain with plastic strain smaller under higher temperatures, thus leading to a weakened nonlinearity of strain-related chord modulus degradation.

Author Statement

JM: Conceptualization, Methodology, Investigation, Formal analysis, Writing - original draft, review and editing. HL: Conceptualization, Methodology, Investigation, Supervision, Writing - review and editing. ZRH: Investigation - experiment, Formal analysis, Writing - review and editing. HY: Investigation – experiment, Writing - review and editing. MWF: Conceptualization, Supervision, Writing - review and editing.

Declaration of competing interest

The authors declare that they have no known competing financial interests or personal relationships that could have appeared to influence the work reported in this paper.

Acknowledgments

This research is supported by the projects from the National Natural Science Foundation of China (51775441, 51835011, 51522509), and the project from the General Research Fund of the Hong Kong Government (15223520). In addition, the authors would like to thank Prof. S.L. Zang at Xi'an Jiaotong University for his insightful suggestions and Dr. S.A.H. Motaman at RWTH Aachen University for his kind help with numerical implementations.

Appendix A. Governing equation for temperature-dependent flow stress

For polycrystalline materials, the shear stress (τ_{y}) during the plastic deformation consists of two components [51], as designated in Eq. (A1).

$$\tau_y = \tau_G + \tau^* \tag{A.1}$$

where τ_{G} is the athermal and rate-independent shear stress from the long-range interactions of dislocation substructures, τ^* is the thermal and rate-dependent shear stress from the short-range referring to the friction resistance to move mobile dislocations across the lattice and pass the obstacles. By taking the Taylor factor into Eq. (A1), it can be further rewritten as the macro scale flow stress.

$$\sigma_y = \sigma_G + \sigma^* \tag{A.2}$$

where σ_G and σ^* are the long-range and short-range stresses, respectively.

Regarding the long-range stress component, it is described as follows [70].

$$\sigma_{\mathrm{G}} = MbG\alpha\sqrt{\rho_{\mathrm{im}}} \tag{A.3}$$

where *G* is the shear modulus, *M* is the Taylor factor, α is a material constant referring to dislocation interaction strength, and the α variation with respect to plastic strain can be neglected [71]. *G* can be further calculated by:

$$G = E/2(1+\nu) \tag{A.4}$$

where *E* is the aforementioned elastic modulus, and *v* is the Poisson's ratio. Burger's vector and Poisson's ratio are less sensitive to temperature and can thus be regarded as constants in cold and warm forming. The elastic modulus and dislocation-related material constant, however, are temperature-dependent [72]. and can be described by various types of equations [73]. In this research, based on the experimental results shown in Fig. 9, a linear relationship is suggested.

For the dislocation-related material constant, the rate sensitivity could be ignored [72], whereas the temperature dependence has to be considered as the dislocation interaction strength is proven to be decreased with the increase of temperature [71]. Therefore, a power function to represent the thermal-activation affected variation of dislocation interaction strength is proposed and denoted as:

$$\frac{\alpha-\alpha_{\text{ref}}}{\alpha_{\text{ref}}}=\lambda_{\alpha}\left(\frac{T-T_{\text{ref}}}{T_{\text{ref}}}\right)^{t} \tag{A.5}$$

where α_{ref} is the reference interaction strength of dislocations, λ_{α} and *t* are the coefficients related to the temperature sensitivity.

As described in Section 4.2, both the cell and wall immobile dislocations contribute to the strain hardening. Due to the different interactions, their contributions to hardening are different. Thus, it is necessary to separately discuss their hardening contributions and the material constants related to dislocation interaction. The total contribution of the two types of immobile dislocations is calculated as the sum of their separated contribution and formulated in Eq. (A6).

$$\sigma_{\text{G}}=\sigma_{\text{G,cell}}+\sigma_{\text{G,wall}}=MbG\left(\alpha_{\text{cell}}\sqrt{\rho_{\text{im-cell}}}+\alpha_{\text{wall}}\sqrt{\rho_{\text{im-wall}}}\right) \tag{A.6}$$

Accordingly, Eq. (A5) can be further designated as

$$\begin{cases}\dfrac{\alpha_{\text{cell}}-\alpha_{\text{ref,cell}}}{\alpha_{\text{ref,cell}}}=r_{\alpha,\text{cell}}\left(\dfrac{T-T_{\text{ref}}}{T_{\text{ref}}}\right)^{tc}\\[2ex] \dfrac{\alpha_{\text{wall}}-\alpha_{\text{ref,wall}}}{\alpha_{\text{ref,wall}}}=r_{\alpha,\text{wall}}\left(\dfrac{T-T_{\text{ref}}}{T_{\text{ref}}}\right)^{tw}\end{cases} \tag{A.7}$$

For the short-range stress component, dislocations must have enough energy to overcome the energy barriers in slipping, and the energy is sensitive to temperature and strain rate. With the increase of temperature or the decrease of strain rate, the shear stress is decreased [54]. The short-range stress is thus described as a function of temperature and strain rate, and a typical one is represented as [74]:

$$\tau^{*}=\tau_{0}\left[1-\left(-\frac{RT}{G_{0}}\ln\frac{\dot{\gamma}_{\text{p}}}{\dot{\gamma}_{\text{ref}}}\right)^{1/q}\right]^{1/p} \tag{A.8}$$

where τ_{0} is the shear stress at the temperature of absolute zero, G_{0} is the free energy for a dislocation to overcome the barrier by thermal activation, $\dot{\gamma}_{\text{p}}$ is calculated by Orowan equation $\dot{\gamma}_{\text{p}}=\rho_{\text{m}}b\overline{v}$, and *p* and *q* are two parameters to define the profile of the short-range barrier [51].

Although the above equation can provide acceptable results in most cases as well as consider physical mechanisms, the temperature-/rate- dependent dislocations mobility behaviors are extremely complex that cannot be fully represented by this equation. In this research, based on the phenomenological approach [53], a modified method is applied to describe the short-range stress component. The rate-dependent viscous stress is determined as:

$$\sigma^{*}/\sigma^{*}_{\text{ref-strain rate}}=\beta^{*}\left(\dot{\varepsilon}_{\text{p}}/\dot{\varepsilon}_{\text{ref-strain rate}}\right)^{s^{*}} \tag{A.9}$$

where $\sigma^*_{\text{ref-strain rate}}$ is the viscous stress at the reference strain rate ($\dot{\varepsilon}_{\text{ref-strain rate}}$), β^* is the coefficient to control the amplitude, and s^* is the strain rate sensitivity which is increased with temperature [51,75]. Moreover, it has been found that the effect of strain rate itself on the sensitivity is very slight [53]. Thus, in the present modeling, the strain rate sensitivity only depends on the forming temperature and thus is described as:

$$\frac{s^* - s^*_{\text{ref}}}{s^*_{\text{ref}}} = \omega_s \left(\frac{T - T_{\text{ref}}}{T_{\text{ref}}} \right)^{r_s} \tag{A.10}$$

Similarly, the temperature dependence can be represented as:

$$\frac{\sigma^* - \sigma^*_{\text{ref-temp}}}{\sigma^*_{\text{ref-temp}}} = \omega^* \left(\frac{T - T_{\text{ref}}}{T_{\text{ref}}} \right)^{r^*} \tag{A.11}$$

where $\sigma^*_{\text{ref-temp}}$ is the viscous stress at the reference temperature, ω^* is the amplitude-related coefficient, and r^* is the exponent coefficient.

By combining the Eqs. (A10) and (A11), temperature- and strain rate-dependent short-range stress components can thus be described as:

$$\sigma^* = \sigma^*_{\text{ref}} \cdot \left[1 + \omega^* \left(\frac{T - T_{\text{ref}}}{T_{\text{ref}}} \right)^{r^*} \right] \cdot \beta^* \left(\frac{\dot{\varepsilon}_{\text{p}}}{\dot{\varepsilon}_{\text{ref}}} \right)^{s^*} \tag{A.12}$$

Appendix B. Numerical and optimization algorithm

The “GlobalSearch” and GA within MATLAB, with a local minimization solver for the constrained nonlinear multivariate functions “fmincon”, is used to achieve the global minimization. The overview of the algorithm is shown in Fig. B1.

In the “GlobalSearch” method, various local minimization algorithms, i.e., interior point, reflective trust region, active set, and SQP, are the potential ones to be used to obtain the local minimization. However, in the present modeling, the evolution rate of dislocation densities cannot be explicitly calculated so a numerical approach should be constructed, and the Forward/Explicit Euler method is applied to realize the numerical integration of various dislocation density evolutions described in Section 4. The detailed expressions are shown in Fig. B1, which are coded by the script of MATLAB. Combining the numerical integration and global optimization algorithm, the final parameters of the model can thus be configured.

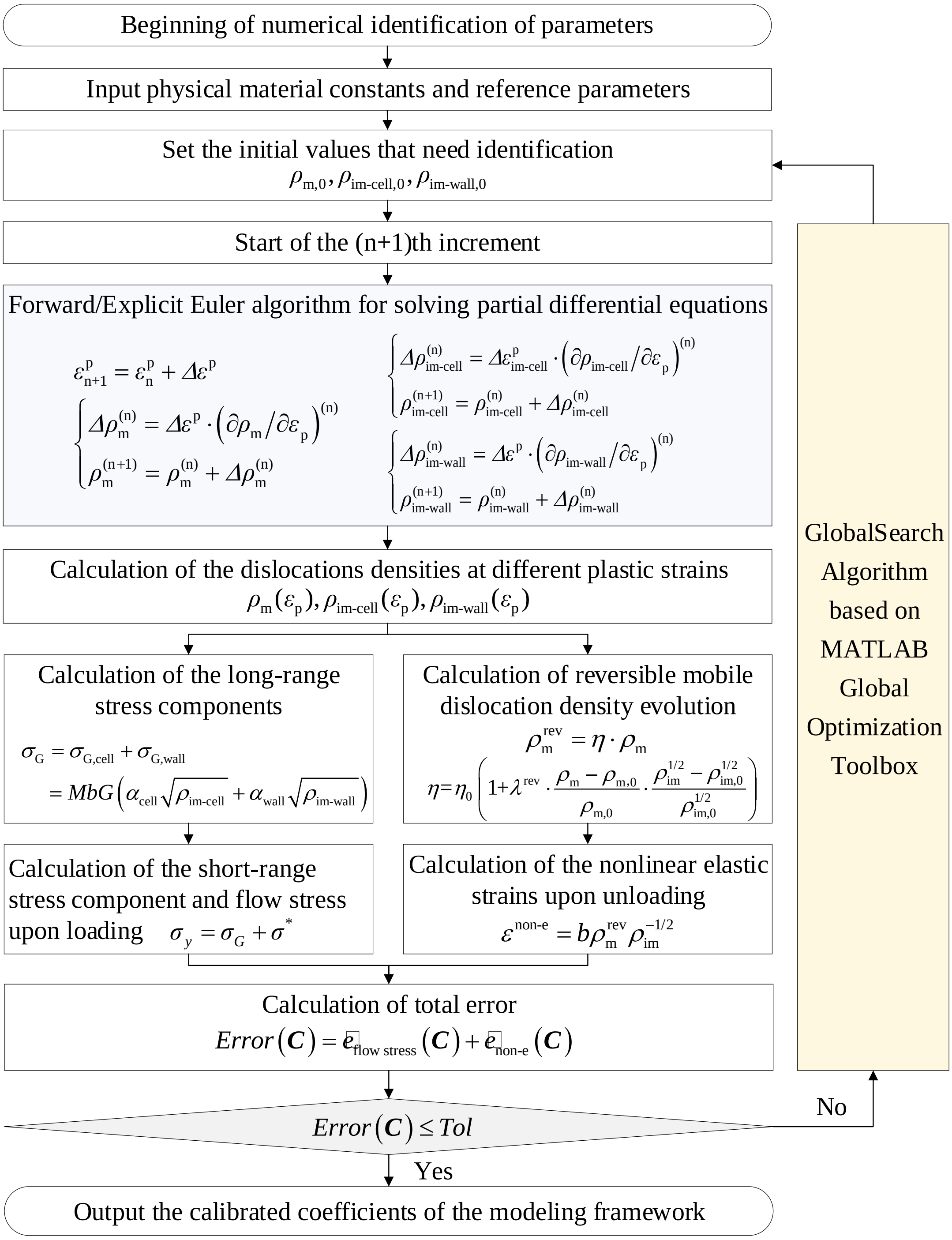

Fig. B.1. Flowchart of the numerical solution and coefficient configuration method.

Appendix C. Coefficients of the model

Table C.1 Dislocation behaviors related coefficients.

$\lambda^{\mathrm{gn}}_{\mathrm{m}}$	$\lambda^{\mathrm{an}}_{\mathrm{m,m}}$	$\lambda^{\mathrm{an}}_{\text{m,im-cell}}$	$\lambda^{\mathrm{an}}_{\text{m,im-wall}}$	$\lambda^{\mathrm{ac}}_{\text{im-cell}}$	$\lambda^{\mathrm{ac}}_{\text{im-wall}}$	$\lambda^{\mathrm{tr}}_{\mathrm{m}}$	$\lambda^{\mathrm{nu}}_{\text{im-cell}}$	$\lambda^{\mathrm{rem}}_{\text{im-cell}}$	$\lambda^{\mathrm{rem}}_{\text{im-wall}}$	$\lambda^{\mathrm{rev}}_{\mathrm{m}}$
0.3996×10^{9}	1.1191×10^{-12}	7.3191×10^{-12}	0.0670×10^{-12}	9.3130×10^{-6}	0.4144×10^{-6}	0.0037×10^{-6}	0.4300×10^{-21}	0.00001	1.1010	3.5677

Table C.2 Physical material constants and reference coefficients.

$\rho_{\mathrm{m},0}$ [m-2]	$\rho_{\text{im-cell},0}$ [m-2]	$\rho_{\text{im-wall},0}$ [m-2]	$\alpha_{\mathrm{cell}}^{\mathrm{ref}}$ [-]	$\alpha_{\mathrm{wall}}^{\mathrm{ref}}$ [-]	$\sigma_{\mathrm{ref}}^{*}$ [MPa]
1.6728×10^{13}	9.9691×10^{11}	6.6348×10^{12}	2.5388	2.6918	649.2330

Table C.3 Temperature sensitivity coefficients.

$\omega_{\text{im-cell}}^{\text{an}}$	$\omega_{\text{im-cell}}^{\text{an}}$	$\omega_{\text{im-wall}}^{\text{an}}$	$\omega_{\mathrm{m}}^{\mathrm{tr}}$	$\omega_{\text{im-wall}}^{\text{nu}}$	$\omega_{\text{im-cell}}^{\text{rem}}$	$\omega_{\text{im-wall}}^{\text{rem}}$	ω_{rev}	$\omega_{\alpha,\mathrm{cell}}$	$\omega_{\alpha,\mathrm{wall}}$	ω^{*}	β^{*}	ω_{s}^{*}
0.4545	0.1932	0.1184	3.0489	0.1029	0.0007	0.0246	0.4098	-0.5000	0.5578	-0.7561	0.3014	0.0001
$r_{\mathrm{m}}^{\mathrm{an}}$	$r_{\text{im-cell}}^{\text{an}}$	$r_{\text{im-wall}}^{\text{an}}$	$r_{\mathrm{m}}^{\mathrm{tr}}$	$r_{\text{im-wall}}^{\text{nu}}$	$r_{\text{im-cell}}^{\text{rem}}$	$r_{\text{im-wall}}^{\text{rem}}$	r_{rev}	$r_{\alpha,\mathrm{cell}}$	$r_{\alpha,\mathrm{wall}}$	r^{*}	s_{ref}^{*}	r_{s}^{*}
2.1478	1.1390	1.4032	7.1610	0.00001	0.0002	0.2353	3.0853	4.2940	3.8889	3.0210	0.0001	0.0001

References

[1] Li H, Fu MW. Deformation-Based Processing of Materials: Behavior, Performance, Modeling, and Control. Elsevier; 2019. https://doi.org/https://doi.org/10.1016/C2017-0-01559-8.

[2] Wagoner RH, Lim H, Lee MG. Advanced issues in springback. Int J Plast 2013;45:3–20. https://doi.org/10.1016/j.ijplas.2012.08.006.

[3] Ma J, Welo T. Analytical springback assessment in flexible stretch bending of complex shapes. Int J Mach Tools Manuf 2021;160:103653. https://doi.org/10.1016/j.ijmachtools.2020.103653.

[4] Ma J, Li H, Fu MW. Modelling of Springback in Tube Bending: A Generalized Analytical Approach. Int J Mech Sci 2021;204:106516. https://doi.org/10.1016/j.ijmecsci.2021.106516.

[5] Morestin F, Boivin M. On the necessity of taking into account the variation in the Young modulus with plastic strain in elastic-plastic software. Nucl Eng Des 1996;162:107–16. https://doi.org/10.1016/0029-5493(95)01123-4.

[6] Ma J, Yang H, Li H, Tao ZJ, Li GJ. Springback prediction of titanium tube bending considering Bauschinger effect and Young's modulus variation. J. Phys. Conf. Ser., vol. 734, 2016. https://doi.org/10.1088/1742-6596/734/3/032113.

[7] Hama T, Matsudai R, Kuchinomachi Y, Fujimoto H, Takuda H. Non-linear Deformation Behavior during Unloading in Various Metal Sheets. ISIJ Int 2015;55:1067–75. https://doi.org/10.2355/isijinternational.55.1067.

[8] Li D, Wagoner RH. The Nature of Yielding and Anelasticity in Metals. Acta Mater 2021:116625. https://doi.org/10.1016/j.actamat.2021.116625.

[9] Choi Y, Lee J, Panicker SS, Jin HK, Panda SK, Lee MG. Mechanical properties, springback, and formability of W-temper and peak aged 7075 aluminum alloy sheets: Experiments and modeling. Int J Mech Sci 2020;170:105344. https://doi.org/10.1016/J.IJMECSCI.2019.105344.

[10] Zang SL, Lee MG, Hoon Kim J. Evaluating the significance of hardening behavior and unloading modulus under strain reversal in sheet springback prediction. Int J Mech Sci 2013;77:194–204. https://doi.org/10.1016/J.IJMECSCI.2013.09.033.

[11] Li G, He Z, Ma J, Yang H, Li H. Springback Analysis for Warm Bending of Titanium Tube Based on Coupled Thermal-Mechanical Simulation. Materials (Basel) 2021;14.

[12] Yang H, Li H, Ma J, Li G, Huang D. Breaking bending limit of difficult-to-form titanium tubes by differential heating-based reconstruction of neutral layer shifting. Int J Mach Tools Manuf 2021;166:103742.

[13] Sun L, Wagoner RH. Complex unloading behavior: Nature of the deformation and its consistent constitutive representation. Int J Plast 2011;27:1126–44. https://doi.org/10.1016/j.ijplas.2010.12.003.

[14] Xue X, Liao J, Vincze G, Pereira ABAB, Barlat F. Experimental assessment of nonlinear elastic behaviour of dual-phase steels and application to springback prediction. Int J Mech Sci 2016;117:1–15. https://doi.org/10.1016/j.ijmecsci.2016.08.003.

[15] Deng N, Kuwabara T, Korkolis YP. On the non-linear unloading behavior of a biaxially loaded dual-phase steel sheet. Int J Mech Sci 2018;138–139:383–97. https://doi.org/10.1016/J.IJMECSCI.2018.02.015.

[16] Pérez R, Benito JA, Prado JM. Study of the inelastic response of TRIP steels after plastic deformation. ISIJ Int 2005;45:1925–33. https://doi.org/10.2355/isijinternational.45.1925.

[17] Hou H, Zhao G, Chen L, Li H. Anisotropic springback models of FCC metal material under severe plastic compressive deformation. Int J Mech Sci 2021;202–203:106513. https://doi.org/10.1016/J.IJMECSCI.2021.106513.

[18] He W, Wan M, Meng B. Size effect on nonlinear unloading behavior and Bauschinger effect of Ni-based superalloy ultrathin sheet. Int J Mech Sci 2022;231:107563. https://doi.org/10.1016/J.IJMECSCI.2022.107563.

[19] Chen Z, Bong HJ, Li D, Wagoner RH. The elastic-plastic transition of metals. Int J Plast 2016;83:178–201. https://doi.org/10.1016/j.ijplas.2016.04.009.

[20] Lim H, Lee MG, Sung JH, Kim JH, Wagoner RH. Time-dependent springback of advanced high strength steels. Int J Plast 2012;29:42–59. https://doi.org/10.1016/j.ijplas.2011.07.008.

[21] Hama T, Suzuki T, Nakatsuji Y, Sakai T, Takuda H. Time-dependent springback of various sheet metals: An experimental study. Mater Trans 2020;61:941–7. https://doi.org/10.2320/matertrans.MT-M2019283.

[22] Li H, Zhang L, Chen G, Ma J, Wei D. Time-dependent springback of high strength titanium tubular materials : Experiment and modeling. J Mater Process Tech 2022;299:117354. https://doi.org/10.1016/j.jmatprotec.2021.117354.

[23] Powell BE, Skove MJ. A combination of third-order elastic constants of aluminum. J Appl Phys 1982;53:164–765.

[24] Hill R. A theory of the yielding and plastic flow of anisotropic metals. Proc R Soc London Ser A Math Phys Sci 1948;193:281–97. https://doi.org/10.1098/rspa.1948.0045.

[25] Wang H, Wu PD, Wang J. Modeling inelastic behavior of magnesium alloys during cyclic loading-unloading. Int J Plast 2013;47:49–64. https://doi.org/10.1016/j.ijplas.2013.01.007.

[26] Tekkaya. Damage in metal forming. CIRP Ann 2020;35:1–24. https://doi.org/10.1016/j.cirp.2020.05.005.

[27] Hama T, Kitamura N, Takuda H. Effect of twinning and detwinning on inelastic behavior during unloading in a magnesium alloy sheet. Mater Sci Eng A 2013;583:232–41. https://doi.org/10.1016/J.MSEA.2013.06.070.

[28] van Liempt P, Sietsma J. A physically based yield criterion I. Determination of the yield stress based on analysis of pre-yield dislocation behaviour. Mater Sci Eng A 2016;662:80–7. https://doi.org/10.1016/j.msea.2016.03.013.

[29] Cleveland RM, Ghosh AK. Inelastic effects on springback in metals. Int J Plast 2002;18:769–85.

[30] Yoshida F, Uemori T. A model of large-strain cyclic plasticity and its application to springback simulation. Int J Mech Sci 2003;45:1687–702. https://doi.org/10.1016/J.IJMECSCI.2003.10.013.

[31] Lee J-Y, Lee M-G, Barlat F, Bae G. Piecewise linear approximation of nonlinear unloading-reloading behaviors using a multi-surface approach. Int J Plast 2017;93:112–36. https://doi.org/10.1016/j.ijplas.2017.02.004.

[32] Hama T, Sakai T, Fujisaki Y, Fujimoto H, Takuda H. Time-dependent springback of a commercially pure titanium sheet. Procedia Eng 2017;207:263–8. https://doi.org/10.1016/j.proeng.2017.10.772.

[33] Andar MO, Kuwabara T, Yonemura S, Uenishi A. Elastic-plastic and inelastic characteristics of high strength steel sheets under biaxial loading and unloading. ISIJ Int 2010;50:613–9. https://doi.org/10.2355/isijinternational.50.613.

[34] Chatti S. Modeling of the elastic modulus evolution in unloading-reloading stages. Int J Mater Form 2013;6:93–101. https://doi.org/10.1007/s12289-011-1075-2.

[35] Yoshida F, Uemori T. A model of large-strain cyclic plasticity describing the Bauschinger effect and workhardening stagnation. Int J Plast 2002;18:661–86. https://doi.org/10.1016/S0749-6419(01)00050-X.

[36] Lee JY, Lee MG, Barlat F, Bae G. Piecewise linear approximation of nonlinear unloading-reloading behaviors using a multi-surface approach. Int J Plast 2017;93:112–36. https://doi.org/10.1016/j.ijplas.2017.02.004.

[37] Lee E-HH, Stoughton TB, Yoon JW. A new strategy to describe nonlinear elastic and asymmetric plastic behaviors with one yield surface. Int J Plast 2017;98:217–38. https://doi.org/10.1016/j.ijplas.2017.08.003.

[38] Arechabaleta Z, Van Liempt P, Sietsma J. Quantification of dislocation structures from anelastic deformation behaviour. Acta Mater 2016;115:314–23. https://doi.org/10.1016/j.actamat.2016.05.040.

[39] Torkabadi A, Perdahcıoğlu ES, Meinders VT, van den Boogaard AH. On the nonlinear anelastic behavior of AHSS. Int J Solids Struct 2018;151:2–8.

https://doi.org/10.1016/J.IJSOLSTR.2017.03.009.

[40] Balland P, Tabourot L, Bizet L, Sene NA, Depres C, Balan T, et al. Young's Modulus Determination: Influence of Microplasticity and Pseudo-Elasticity on Metal Forming. Key Eng Mater 2015;651–653:598–603. https://doi.org/10.4028/www.scientific.net/KEM.651-653.598.

[41] Rajput A, Paul SK. Understanding the physics of non-linear unloading-reloading behavior of metal for springback prediction. J Mol Model 2019;25:321. https://doi.org/10.1007/s00894-019-4203-4.

[42] AMS SAE 4946. Titanium Alloy Tubing, Seamless, Hydraulic 3Al - 2.5V, Texture Controlled Cold Worked, Stress Relieved 2010.

[43] Bridier F, Villechaise P, Mendez J. Analysis of the different slip systems activated by tension in a α/β titanium alloy in relation with local crystallographic orientation. Acta Mater 2005;53:555–67. https://doi.org/10.1016/J.ACTAMAT.2004.09.040.

[44] Li H, Zhang HQ, Yang H, Fu MW, Yang H. Anisotropic and asymmetrical yielding and its evolution in plastic deformation: Titanium tubular materials. Int J Plast 2017;90:177–211. https://doi.org/10.1016/j.ijplas.2017.01.004.

[45] ASTM E8/E8M-21. Standard Test Methods for Tension Testing of Metallic Materials 2013.

[46] ASTM E21. Standard Test Methods for Elevated Temperature Tension Tests of Metallic Materials 2013.

[47] Eggertsen PA, Mattiasson K. On constitutive modeling for springback analysis. Int J Mech Sci 2010;52:804–18. https://doi.org/10.1016/j.ijmecsci.2010.01.008.

[48] Zhu YX, Chen W, Li HP, Liu YL, Chen L. Springback study of RDB of rectangular H96 tube. Int J Mech Sci 2018;138–139:282–94. https://doi.org/10.1016/j.ijmecsci.2018.02.022.

[49] Physics M, Faculty P. Temperature Dependence of Young's Modulus of a-Titanium Polycrystals. Phys Stat Sol 1994;75:75–7.

[50] Huang K. On the atomic theory of elasticity. Trans Faraday Soc 1950;203:178–194.

[51] Kocks UF. Laws for Work-Hardening and Low-Temperature Creep. J Eng Mater Technol 1976;98:76–85. https://doi.org/10.1115/1.3443340.

[52] Clayton JD, McDowell DL, Bammann DJ. Modeling dislocations and disclinations with finite micropolar elastoplasticity. Int J Plast 2006;22:210–56. https://doi.org/10.1016/J.IJPLAS.2004.12.001.

[53] Motaman SAH, Prahl U. Microstructural constitutive model for polycrystal viscoplasticity in cold and warm regimes based on continuum dislocation dynamics. J Mech Phys Solids 2019;122:205–43. https://doi.org/10.1016/J.JMPS.2018.09.002.

[54] Hull D, Bacon DJ. Chapter 3 - Movement of Dislocations. In: Hull D, Bacon DJBT-I to D (Fifth E, editors. Introd. to Dislocations, Oxford: Butterworth-Heinemann; 2011, p. 43–62. https://doi.org/https://doi.org/10.1016/B978-0-08-096672-4.00003-7.

[55] Kim H, Kim C, Barlat F, Pavlina E, Lee MG. Nonlinear elastic behaviors of low and high strength steels in unloading and reloading. Mater Sci Eng A 2013;562:161–71. https://doi.org/10.1016/j.msea.2012.11.020.

[56] Torkabadi A, Perdahc ES, Boogaard AH Van Den. Modelling of anelastic deformation in dual-phase steel for improved springback simulation 2017;00:17–22.

[57] Hatem TM, Zikry MA. Shear pipe effects and dynamic shear-strain localization in martensitic steels. Acta Mater 2009;57:4558–67. https://doi.org/https://doi.org/10.1016/j.actamat.2009.06.028.

[58] Kocks UF. A statistical theory of flow stress and work-hardening. Philos Mag A J Theor Exp Appl Phys 1966;13:541–66. https://doi.org/10.1080/14786436608212647.

[59] Frank FC, Read WT. Multiplication Processes for Slow Moving Dislocations. Phys Rev 1950;79:722–3. https://doi.org/10.1103/PhysRev.79.722.

[60] Ghosh AK. A physically-based constitutive model for metal deformation. Acta Metall 1980;28:1443–65. https://doi.org/10.1016/0001-6160(80)90046-2.

[61] Steif PS, Clifton RJ. On the kinetics of a Frank-Read source. Mater Sci Eng 1979;41:251–8. https://doi.org/https://doi.org/10.1016/0025-5416(79)90145-9.

[62] He X, Liu L, Zeng T, Yao Y. Micromechanical modeling of work hardening for coupling microstructure evolution, dynamic recovery and recrystallization: Application to high entropy alloys. Int J Mech Sci 2020;177:105567. https://doi.org/10.1016/J.IJMECSCI.2020.105567.

[63] Stricker M, Sudmanns M, Schulz K, Hochrainer T, Weygand D. Dislocation multiplication in stage II deformation of fcc multi-slip single crystals. J Mech Phys Solids 2018;119:319–33. https://doi.org/10.1016/J.JMPS.2018.07.003.

[64] Ananthakrishna G, Sahoo D. A model based on nonlinear oscillations to explain jumps on creep curves. J Phys D Appl Phys 1981;14:2081–90. https://doi.org/10.1088/0022-3727/14/11/015.

[65] Bergström Y. A dislocation model for the stress-strain behaviour of polycrystalline α-Fe with special emphasis on the variation of the densities of mobile and immobile dislocations. Mater Sci Eng 1970;5:193–200. https://doi.org/https://doi.org/10.1016/0025-5416(70)90081-9.

[66] Schowtjak A, Schulte R, Clausmeyer T, Ostwald R, Tekkaya AE, Menzel A. ADAPT — A Diversely Applicable Parameter Identification Tool: Overview and full-field application examples. Int J Mech Sci 2021:106840. https://doi.org/10.1016/J.IJMECSCI.2021.106840.

[67] Becker H, Pantleon W. Work-hardening stages and deformation mechanism maps during tensile deformation of commercially pure titanium. Comput Mater Sci 2013;76:52–9. https://doi.org/https://doi.org/10.1016/j.commatsci.2013.03.028.

[68] Arechabaleta Z, van Liempt P, Sietsma J. Unravelling dislocation networks in metals. Mater Sci Eng A 2017;710:329–33. https://doi.org/10.1016/j.msea.2017.10.099.

[69] van Liempt P, Bos C, Sietsma J. A physically based yield criterion II. Incorporation of Hall Petch effect and resistance due to thermally activated dislocation glide. Mater Sci Eng A 2016;652:7–13. https://doi.org/10.1016/j.msea.2015.11.035.

[70] Seeger A. The generation of lattice defects by moving dislocations, and its application to the temperature dependence of the flow-stress of F.C.C. crystals. London, Edinburgh,

Dublin Philos Mag J Sci 1955;46:1194–217. https://doi.org/10.1080/14786441108520632.

[71] Kocks UF, Mecking H. Physics and phenomenology of strain hardening: The FCC case. Prog Mater Sci 2003;48:171–273. https://doi.org/10.1016/S0079-6425(02)00003-8.

[72] Mecking H, Kocks UF. Kinetics of flow and strain-hardening. Acta Metall 1981;29:1865–75. https://doi.org/https://doi.org/10.1016/0001-6160(81)90112-7.

[73] Rusinek A, Rodríguez-Martínez JA. Thermo-viscoplastic constitutive relation for aluminium alloys, modeling of negative strain rate sensitivity and viscous drag effects. Mater Des 2009;30:4377–90. https://doi.org/https://doi.org/10.1016/j.matdes.2009.04.011.

[74] Cheng J, Nemat-Nasser S. A model for experimentally-observed high-strain-rate dynamic strain aging in titanium. Acta Mater 2000;48:3131–44. https://doi.org/https://doi.org/10.1016/S1359-6454(00)00124-5.

[75] Cereceda D, Diehl M, Roters F, Raabe D, Perlado JM, Marian J. Unraveling the temperature dependence of the yield strength in single-crystal tungsten using atomistically-informed crystal plasticity calculations. Int J Plast 2016;78:242–65. https://doi.org/https://doi.org/10.1016/j.ijplas.2015.09.002.